

Measurement of $\bar{\nu}_\mu$ charged-current single π^- production on hydrocarbon in the few-GeV region using MINERvA

T. Le,^{1,2} F. Akbar,³ L. Aliaga,^{4,5} D. A. Andrade,⁶ M. V. Ascencio,⁵ A. Bashyal,⁷ A. Bercelette,⁸ M. Betancourt,⁹ A. Bodek,⁸ J. L. Bonilla,⁶ A. Bravar,¹⁰ H. Budd,⁸ G. Caceres,¹¹ T. Cai,⁸ M. F. Carneiro,⁷ D. Coplewe,¹² S. A. Dytman,¹³ G. A. Díaz,^{8,5} J. Felix,⁶ L. Fields,^{9,14} A. Filkins,⁴ R. Fine,⁸ N. Fiza,¹⁵ A. M. Gago,⁵ H. Gallagher,¹ A. Ghosh,^{16,11} R. Gran,¹⁷ D. A. Harris,⁹ S. Henry,⁸ S. Jena,¹⁵ J. Kleykamp,⁸ M. Kordosky,⁴ D. Last,¹⁸ X.-G. Lu,¹² E. Maher,¹⁹ S. Manly,⁸ W. A. Mann¹, C. Mauger,¹⁸ K. S. McFarland,^{8,9} A. M. McGowan,⁸ B. Messerly,¹³ J. Miller,¹⁶ J. G. Morfín,⁹ D. Naples,¹³ J. K. Nelson,⁴ C. Nguyen,²⁰ A. Norrick,⁴ Nuruzzaman,^{2,16} A. Olivier,⁸ V. Paolone,¹³ G. N. Perdue,^{9,8} M. A. Ramírez,⁶ R. D. Ransome,² H. Ray,²⁰ D. Rimal,²⁰ D. Ruterbories,⁸ H. Schellman,^{7,14} J. T. Sobczyk,²¹ C. J. Solano Salinas,²² H. Su,¹³ M. Sultana,⁸ V. S. Syrotenko,¹ E. Valencia,^{4,6} M. Wospakrik,²⁰ B. Yaeggy,¹⁶ and L. Zazueta⁴

(MINERvA Collaboration)

¹Physics Department, Tufts University, Medford, Massachusetts 02155, USA

²Rutgers, The State University of New Jersey, Piscataway, New Jersey 08854, USA

³AMU Campus, Aligarh, Uttar Pradesh 202001, India

⁴Department of Physics, College of William & Mary, Williamsburg, Virginia 23187, USA

⁵Sección Física, Departamento de Ciencias, Pontificia Universidad Católica del Perú, Apartado 1761, Lima, Perú

⁶Campus León y Campus Guanajuato, Universidad de Guanajuato, Lascurain de Retana No. 5, Colonia Centro, Guanajuato 36000, Guanajuato México

⁷Department of Physics, Oregon State University, Corvallis, Oregon 97331, USA

⁸University of Rochester, Rochester, New York 14627 USA

⁹Fermi National Accelerator Laboratory, Batavia, Illinois 60510, USA

¹⁰University of Geneva, 1211 Geneva 4, Switzerland

¹¹Centro Brasileiro de Pesquisas Físicas, Rua Dr. Xavier Sigaud 150, Urca, Rio de Janeiro, Rio de Janeiro 22290-180, Brazil

¹²Oxford University, Department of Physics, Oxford OX1 3RH, United Kingdom

¹³Department of Physics and Astronomy, University of Pittsburgh, Pittsburgh, Pennsylvania 15260, USA

¹⁴Northwestern University, Evanston, Illinois 60208, USA

¹⁵IISER, Mohali, Knowledge city, Sector 81, Manauli PO 140306

¹⁶Departamento de Física, Universidad Técnica Federico Santa María, Avenida España 1680 Casilla 110-V, Valparaíso, Chile

¹⁷Department of Physics, University of Minnesota - Duluth, Duluth, Minnesota 55812, USA

¹⁸Department of Physics and Astronomy, University of Pennsylvania, Philadelphia, Pennsylvania 19104, USA

¹⁹Massachusetts College of Liberal Arts, 375 Church Street, North Adams, Massachusetts 01247, USA

²⁰University of Florida, Department of Physics, Gainesville, Florida 32611, USA

²¹University of Wrocław, plac Uniwersytecki 1, 50-137 Wrocław, Poland

²²Universidad Nacional de Ingeniería, Apartado 31139, Lima, Perú



(Received 25 June 2019; published 16 September 2019)

The antineutrino scattering channel $\bar{\nu}_\mu \text{CH} \rightarrow \mu^+ \pi^- X$ (nucleon(s)) is analyzed in the incident energy range 1.5 to 10 GeV using the MINERvA detector at Fermilab. Differential cross sections are reported as functions of μ^+ momentum and production angle, π^- kinetic energy and production angle, and antineutrino energy and squared four-momentum transfer. Distribution shapes are generally reproduced by simulations based on the GENIE, NuWro, and GiBUU event generators, however GENIE (GiBUU) overestimates (underestimates) the cross section normalizations by 8% (10%). Comparisons of data with the GENIE-based reference simulation probe conventional treatments of cross sections and pion intranuclear

rescattering. The distribution of nontrack vertex energy is used to decompose the signal sample into reaction categories, and cross sections are determined for the exclusive reactions $\mu^+\pi^-n$ and $\mu^+\pi^-p$. A similar treatment applied to the published MINERvA sample $\bar{\nu}_\mu\text{CH} \rightarrow \mu^+\pi^0X[\text{nucleon(s)}]$ has determined the $\mu^+\pi^0n$ cross section, and the latter is used with $\sigma(\pi^-n)$ and $\sigma(\pi^-p)$ to carry out an isospin decomposition of $\bar{\nu}_\mu$ -induced CC(π). The ratio of magnitudes and relative phase for isospin amplitudes A_3 and A_1 thereby obtained are: $R^{\bar{\nu}} = 0.99 \pm 0.19$ and $\phi^{\bar{\nu}} = 93^\circ \pm 7^\circ$. Our results are in agreement with bubble chamber measurements made four decades ago.

DOI: [10.1103/PhysRevD.100.052008](https://doi.org/10.1103/PhysRevD.100.052008)

I. INTRODUCTION

An international effort is underway to determine the ordering of neutrino mass eigenstates, to delimit the amount of charge conjugation plus parity (CP) violation in the neutrino sector, and to measure the angles that characterize neutrino flavor mixing. To achieve the levels of precision that these goals require, neutrino flavor oscillations must be investigated using $\bar{\nu}_\mu$ as well as ν_μ beams because antineutrino vs neutrino propagation in matter elicits differences that are highly informative. Comparisons of antineutrino vs neutrino oscillations are best carried out using the same long-baseline and source of ν fluxes. This general strategy underwrites the ongoing experimental programs of T2K [1] and NOvA [2], and it strongly shapes the DUNE program [3]. In recent times, combined analyses of ν_μ and $\bar{\nu}_\mu$ oscillations have been reported by T2K and NOvA, with each experiment restricting to its own data [4,5]. These observations allow large values for the Dirac CP -violating phase, and they permit the atmospheric mixing angle θ_{23} to have values in either the lower or upper octant, or to coincide with maximal mixing at 45° . At the present time, an unambiguous picture for the neutrino sector continues to elude. For continued progress, the details of antineutrino-nucleus scattering must be established at a level of accuracy that heretofore has not been available. Such an understanding must encompass $\bar{\nu}_\mu$ scattering on nuclear media used in long baseline experiments, of which hydrocarbon is the simplest representative.

There has been a dearth of measurements for charged current (CC) single pion production by antineutrino-nucleus scattering in the threshold-to-few GeV region of incident $\bar{\nu}_\mu$ energy, $E_{\bar{\nu}}$ [6]. This work addresses the situation by presenting detailed measurements of the semiexclusive antineutrino interaction channel

$$\bar{\nu}_\mu + \text{CH} \rightarrow \mu^+ + \pi^- + X(\text{nucleon(s)}). \quad (1)$$

Here, the hadronic system X may contain any number of protons and neutrons, but no additional mesons. For the selected events, X will consist of an interaction neutron or proton, plus remnant nucleons from breakup of the target nucleus.

Signal channel (1) receives large contributions from two CC exclusive reactions:

$$\bar{\nu}_\mu + n \rightarrow \mu^+ + \pi^- + n, \quad (2)$$

and

$$\bar{\nu}_\mu + p \rightarrow \mu^+ + \pi^- + p. \quad (3)$$

The scattering is dominated by interactions within carbon nuclei, however reaction (3) can take place on hydrogen as well. The signal channel is affected by migrations to and from other channels as the result of nuclear medium effects. For example, intranuclear absorption of π^- mesons initially created by channel (1) within carbon nuclei depletes the signal-channel rate that would otherwise be obtained if the interactions occurred on free nucleons. On the other hand, CC multipion production followed by intranuclear pion absorption gives a rate enhancement to the observable (out of parent nucleus) final states of channel (1) that originates from reactions that are not as-born CC single π^- occurrences. Additionally, charge exchange within the struck nucleus can move events out of or into ($\pi^-p \leftrightarrow \pi^0n$) channel (1).

Channel (1) receives a small contribution from CC coherent single π^- production wherein an incident $\bar{\nu}_\mu$ scatters from the entire target nucleus:

$$\bar{\nu}_\mu + \mathcal{A} \rightarrow \mu^+ + \pi^- + \mathcal{A}, \quad (4)$$

The cross section for reaction (4) on carbon has been previously measured by MINERvA [7,8].

The CC interactions that comprise channel (1) are of keen interest to the NOvA and T2K analyses of $\bar{\nu}_\mu$ oscillations, since antineutrino CC(1π) channels give significant event rates in the one to few-GeV region of $E_{\bar{\nu}}$. This $E_{\bar{\nu}}$ range is affected by ν_e flavor appearance and ν_μ flavor disappearance over the long baselines used by these experiments, and this will also be the case for the next-generation long-baseline oscillation experiments, DUNE and Hyper-Kamiokande [9].

The analysis presented here obtains differential cross sections for channel (1) that characterize the kinematics of both the final-state μ^+ and the produced π^- . These differential cross sections complement and extend MINERvA's previously reported measurements of CC pion

production on hydrocarbon. The latter measurements include $\bar{\nu}_\mu$ -induced $\text{CC}(1\pi^0)$ production [10,11], and ν_μ -induced $\text{CC}(\pi^+)$ and $\text{CC}(1\pi^0)$ production [11–13].

A. $\bar{\nu}_\mu$ - $\text{CC}(\pi^-)$ measurements and phenomenology

Current knowledge concerning channel (1) and reactions (2) and (3) is based on bubble chamber antineutrino experiments of the 1970s and 1980s. Cross sections for reactions (2) and (3) taking place in propane + freon mixtures were obtained in the few-GeV region ($\langle E_{\bar{\nu}} \rangle = 1.5$ GeV) using Gargamelle [14,15] and over the range 3 to 30 GeV using SKAT [16]. Investigations of both reactions for incident $\bar{\nu}_\mu$ energies exceeding 5 GeV were carried out using large deuterium-filled bubble chambers [17–19], and reaction (3) was studied over the range $5 < E_{\bar{\nu}} < 120$ GeV using BEBC with a hydrogen fill [20]. The relative contributions from baryon resonances was found to be rather different in the two exclusive reactions: Reaction (2) is an $I = 3/2$ channel in which production of the $\Delta^-(1232)$ resonance plays a major role, while (3) contains $I = 1/2$ as well as $I = 3/2$ amplitudes. For reaction (3) at multi-GeV incident energies, production of $I = 1/2$ baryon resonances—the $N^*(1520)$, $N^*(1535)$, and higher mass N^* states—was reported to be comparable to Δ production.

Event samples recorded by the bubble chamber experiments were often limited to a few hundred events. The present work benefits from higher statistics afforded by MINERvA exposures to the intense, low energy NuMI antineutrino beam at Fermilab [21]. Furthermore it is carried out for an $E_{\bar{\nu}}$ range that intersects the T2K range and spans the ranges of NOvA, and DUNE, and it utilizes a hydrocarbon target medium whose nuclear composition is very close to that of the NOvA detectors while also approximating the target media used by T2K.

Neutrino experimentation has benefitted from a recent surge in theoretical studies that address neutrino-induced $\text{CC}(1\pi)$ production [6]. On the other hand, antineutrino $\text{CC}(1\pi)$ production on nuclei has received a relatively limited treatment [22–24], although the situation is improving [25–28]. To date, $\bar{\nu}_\mu$ -induced pion distributions in momentum and in production angle have been predicted for MINERvA based upon the GIBUU neutrino generator [24], and cross sections on nuclei for $0.5 \leq E_{\bar{\nu}} \leq 3.0$ GeV have been predicted for reactions (2) and (3) [23]. For the latter two reactions as they occur on quasifree nucleons, the classic Rein-Sehgal treatment [29,30] provides a phenomenological framework which is assimilated into several of the current neutrino event generators.

II. OVERVIEW OF DATA AND ANALYSIS

A. Detector, exposure, and $\bar{\nu}$ flux

Interactions of muon antineutrinos from the NuMI beam at Fermilab [21] were recorded in the fine-grained

plastic-scintillator tracking detector of MINERvA [31,32]. The detector’s central tracking region is surrounded by electromagnetic and hadronic calorimeters, providing event containment. The magnetized MINOS near detector, located 2 m downstream of MINERvA, serves as the muon spectrometer [33]. The analysis uses a hexagonal cross section fiducial volume of 2.0 m minimal diameter that extends 2.4 m along the beam direction and has a mass of 5570 kg. The fiducial volume consists of 112 planes composed of polystyrene scintillator strips with triangular cross sections of 1.7 cm height, 3.3 cm width, laid transversely to the detector’s horizontal axis. The planes of the central tracking region (“tracker”) are configured in modules with two planes per module; an air gap of 2.5 mm separates each module. The detector horizontal axis is inclined at 3.34° relative to the beam direction. Three scintillator-plane orientations, at 0° and $\pm 60^\circ$ relative to the detector vertical axis, provide X, U, and V “views” of interactions in the scintillator. The planes alternate between UX and VX pairs, enabling 3-D reconstruction of interaction vertices, charged tracks, and electromagnetic showers. Surrounding the downstream and outer side surfaces of the central tracker are the tracking layers of the electromagnetic and hadronic calorimeters, designated ECAL and HCAL, respectively. The ECAL regions lie within the HCAL and are in contact with the outer layers of the central tracker. The ECAL is of similar construction to the central tracker but includes a 0.2 cm (0.35 radiation length) lead sheet in front of every plane of scintillator. The HCAL surrounds the ECAL; it consists of alternating layers of scintillator and 2.54 cm thick steel plates. The readout electronics have a timing resolution of 3.0 ns for hits of minimum ionizing particles [34], enabling efficient separation of multiple interactions within a single $10 \mu\text{s}$ beam spill.

A μ^+ that exits the downstream surface of MINERvA is tracked by the magnetized, steel-plus-scintillator planes of MINOS, and its momentum and charge are measured. Trajectories of individual muons traversing the two detectors are matched together by correlating the positions, angles, and timings of track segments in each detector.

The data were taken between September 2010 and May 2012 using the low-energy NuMI mode, which produces a wide-band beam with antineutrino energies extending from 1 GeV to greater than 20 GeV and a peak energy of 3 GeV. The polarity of current in the magnetic horns in the beamline was set to focus π^- mesons, providing a $\bar{\nu}_\mu$ enhanced flux with an exposure of 1.06×10^{20} protons on target (POT).

The $\bar{\nu}_\mu$ flux is calculated using a detailed simulation of the NuMI beamline based on GEANT4 [35,36] v9.2.p03 with the FTFP_BERT physics list. The simulation is constrained using proton-carbon yield measurements [37–39] together with more recent thin-target data on hadron yields [40]. A further constraint is derived using

the $\nu + e^-$ scattering rate observed by MINERvA [41]. Additional details as pertain to the antineutrino exposures of this work can be found in Ref. [42].

B. Neutrino interaction modeling

The reference Monte Carlo (MC) simulation used by this analysis is built upon the GENIE 2.8.4 neutrino event generator [43]. The rendering of antineutrino-nucleus interactions is based upon the same GENIE models described in Ref. [42]. Additional details concerning GENIE modeling of CC(π) channels are given in MINERvA publications [11–13]. Recent developments in neutrino phenomenology motivate certain augmentations to GENIE that are implemented via event reweighting and by adding a simulated sample of quasielastic-like 2-particle 2-hole (2p2h) events [44]. The refinements (described below) are very similar to those used in the reference simulations of recent, published MINERvA measurements [8,13,42,45–49]. Importantly, all refinements to the GENIE-based MC used here (version designation MnvGENIE v1.2) were decided prior to the present work, and the data analyzed here were not used in the GENIE tuning.

In brief, the struck nucleus is treated as a relativistic Fermi gas augmented with a high-momentum tail that accounts for short-range correlations [50]. Antineutrino-induced pion production arises from interaction with single nucleons and proceeds either by baryon-resonance excitation (RES) or by nonresonant deep inelastic scattering (DIS). Simulation of baryon resonance pion production is based upon the Rein-Sehgal model [29], updated with modern baryon-resonance properties [51]. Decays of baryon resonances produced by antineutrinos are generated isotropically in their rest frames. Interference among baryon-resonance amplitudes is assumed to be absent.

Concerning nonresonant single pion production, the Rein-Sehgal formalism is not used. Instead, the rate of nonresonant pion production is assigned according to the formalism of Bodek-Yang [52] with parameters adjusted to reproduce electron and neutrino scattering measurements over the invariant hadronic mass range $W < 1.7$ GeV [53–55]. The total charge of nonresonant pion-nucleon states is constrained by charge conservation. For antineutrino CC interactions, if the final-state pion-nucleon total charge is -1 , then the particle content is always π^-n . But if the total charge is zero, then the particle content is assigned to be π^-p or π^0n with probability $2/3$ or $1/3$, respectively.

An accurate accounting of intranuclear final-state interactions (FSI) for pions and nucleons is important for this analysis. This is because of the large pion-nucleon cross sections that occur in the vicinity of Δ -resonance excitation. The GENIE-based simulation however, does not invoke a microscopic cascade involving formation, propagation, interaction, and medium modification of Δ states. Instead it uses an effective particle cascade in which each final-state pion or nucleon is allowed to have at most one

rescattering interaction before being absorbed or exiting the target nucleus. The relative probabilities among scattering processes are assigned according to pion-nucleus scattering data [56]. This approach is amenable to simple event reweighting, whereas a full particle cascade is much more involved because weights need to be varied for every produced hadron. The effective cascade approach works well with relatively low- A nuclei such as carbon and oxygen. Its predictions give good descriptions of FSI distortions observed in pion distributions by MINERvA studies of CC single pion production [10–13].

For antineutrino CC pion production, a rate reduction scale factor of 0.50 ± 0.50 has been applied to the default GENIE prediction for the nonresonant pion contribution. Such a reduction has been shown to improve the agreement between GENIE and ν_μ -deuterium bubble chamber data [54,55], and it also improves the data-versus-MC agreement in the present analysis.

Antineutrino quasielastic-like (QE-like) reactions are minor sources of background for signal channel (1). Nevertheless, QE-like rate enhancement induced by 2p2h processes is addressed by adding 2p2h events to the reference simulation. Their generation is based on the Valencia model [57,58], but with the interaction rate raised in order to match the data rate observed in MINERvA inclusive ν_μ scattering data [44]. This tuning of the 2p2h component gives a prediction that well-describes MINERvA $\bar{\nu}_\mu$ CC data for both inclusive low three-momentum transfer [47] and exclusive zero-pion samples [42]. Additionally, kinematic distortions of QE-like events that arise from long-range nucleon-nucleon correlations are included in accord with the random phase approximation (RPA) calculations given in Ref. [59].

Simulation of the coherent CC pion-production reaction (4) is based on the Rein-Sehgal model [60], with parameters tuned to give agreement with MINERvA measurements for this channel [8].

C. Predictions using NuWro and GiBUU

For all differential cross sections measured in this work, comparisons are made to the predictions of the GENIE-based reference simulation. Alternate perspectives are provided using the predictions of NuWro [61] and of the 2017 release of GiBUU [62,63]. These are two completely independent event generators whose physics models differ in many ways from those of GENIE.

In NuWro, $\Delta(1232)$ production is calculated using the Adler model [64,65] instead of relying on the Rein-Sehgal phenomenology. The baryon-resonance region extends to $W < 1.6$ GeV; nonresonant pion production is added incoherently as a fraction of DIS, where DIS is based upon the Bodek-Yang model [52]. Hadronic FSI within parent nuclei are fully treated. NuWro simulates pion and nucleon FSI using the cascade formalism of the Salcedo-Oset model [66].

It also accounts for nuclear-medium modification of Δ states [67].

In GiBUU, baryon-resonance production and nonresonant pion production are broken out into their vector and axial vector components. The vector currents are fully determined by electron-nucleus scattering data (MAID 2007 [68]). The axial-vector parts are modeled using partially conserved axial currents (PCAC) and a dipole form factor or a modified dipole form in the case of the $\Delta(1232)$ [69], with an axial-vector mass of 1.0 GeV. Strengths of the axial-vector parts are set according to pion production data. Nonresonant scattering for hadronic masses below the Δ is treated according to effective field theory. The nuclear model of GiBUU uses a relativistic local Fermi gas to characterize the momenta of nucleons bound within a potential characterized by a realistic density function. The hadronic FSI treatment is based on relativistic transport theory [63]. The GiBUU version used by this analysis, hereafter referred to as GiBUU-2017, does not include the CC coherent reaction (4), and an estimate of its contribution based upon MINERvA measurements has been added to its predictions. Also, the 2017 version does not contain background contributions to $\bar{\nu}_\mu$ pion production (as are included in a 2019 release [63]).

D. Detector calibrations and event isolation

The ionization response of the MINERvA detector to muons and charged hadrons is simulated using GEANT4 [35,36] v4.9.4p02 with the QGSP_BERT physics list. The ionization energy scale is established by requiring the simulation to match reconstructed energies deposited by throughgoing muons that have been momentum-analyzed using the magnetized tracking volume of MINOS [31]. For muon dE/dx energy loss, this scale is known to within 2%. For hadronic ionization energy deposits (“hits”), the energy assigned in reconstruction makes use of calorimetric corrections. The corrections were initially extracted from simulations [31] and subsequently refined and validated using measurements obtained with a scaled-down replicate detector operated in a low-energy particle test beam [32]. The test beam data, in conjunction with *in-situ* measurements, enable determinations of tracking efficiencies and energy responses to charged pions, protons, and electrons, and establish the value of Birks’ constant that best describes the scintillator’s light yield.

For each 10 μs spill window of the NuMI antineutrino beam, ionization hits in the scintillator are isolated in time using “time slices” of tens to sub-two-hundred nanoseconds. As a result, each antineutrino event is associated with a unique time slice. Charged particles initiated by an event traverse the scintillator strips of the central tracker, and their trajectories are recorded as individual hits with specific charge content and time of occurrence. These ionization hits are grouped in time, and neighboring hits in each scintillator plane are gathered into “clusters.” Clusters

having more than 1 MeV of energy are matched among the three views and tracks are reconstructed from them. The reconstructions achieve a position resolution per plane of 2.7 mm, and a track angular resolution of better than 10 mrad in each view [31].

III. TRACK RECONSTRUCTION AND ENERGY ESTIMATION

A track of a candidate CC interaction in the central tracker is designated as the final-state μ^+ if it exits MINERvA’s downstream surface and can be matched with a positively-charged track entering the upstream face of MINOS. Candidate muons are required to have production angles $\theta_\mu < 25^\circ$ relative to the beam direction to ensure that they propagate through the MINOS magnetized volume.

Muon reconstruction uses the trajectory segments in both MINERvA and MINOS to achieve a momentum resolution (σ of the residual fractional error) that increases gradually from 3.6% below 2 GeV/c to 7.9% above 6 GeV/c. With the reconstruction of muon tracks, there is a small mis-modeling of the efficiency for building single trajectories that traverse both MINERvA and MINOS. This is addressed by applying a downwards correction of -4.4% (-1.1%) to the simulated efficiency for muons of momenta less than (greater than) 3 GeV/c [11]. Upon reconstruction of the μ^+ track in an event, the primary vertex location is estimated using the most upstream hit of the muon and a search is made for shorter, hadronic tracks associated with the primary vertex. Additional tracks that are found are reconstructed and the vertex position is refit. Candidate events are required to have primary vertices that occur within the central 112 planes of the scintillator tracking region and are located at least 22 cm away from any edge of the planes. These requirements define the vertex fiducial volume whose target mass is 5.57 metric tons and contains 3.41×10^{30} nucleons.

Events with no reconstructed tracks from the primary vertex other than the muon are removed from the analysis. For the remaining events, it is required that one and only one charged hadronic track accompanies the μ^+ . The latter tracks may initiate secondary interactions that appear as “kinks” along their trajectories. In order to associate all ionizations from secondary scatters with the originating track, searches are made for additional track segments starting at the endpoints of tracks already reconstructed. The pattern of hit ionizations for the hadronic track is then examined for compatibility with charged pion and proton hypotheses. That is, the ionization dE/dx profile is compared to profiles for charged pions and for protons calculated using the Bethe-Bloch formula, and a particle type is assigned according to likelihood ratios. An event is retained if the nonmuon track is identified in this way as being a charged pion. Based on its ionization, on the constraint of charge conservation, and on the apparent

absence of a Michel electron from π^+ decay (see below), such a track is highly likely (probability $\simeq 0.96$) to be a π^- .

The pion kinetic energy, T_{π^-} , is assigned according to total track range, and the distribution of T_{π^-} is subsequently corrected for residual missing energy using an unfolding procedure (see Sec. X). For event-by-event estimation of E_{π} however, energy from range is augmented by a sum over ionization hits coincident with the event that lie away from but in proximity to the π^- track. Such hits are reconstructed according to the detector's calibrated calorimetric response and are designated as E_{π}^{calo} . Hits that comprise E_{π}^{calo} are required to be >10 cm away from the primary vertex and to lie within a radius of 65 cm around the endpoint of the π^- track. With this search radius, approximately 83% of off-track pion-induced ionizations are captured, while $\sim 50\%$ of final-state nucleon-induced hits are excluded. In this way, contamination into E_{π}^{calo} from neutron scatters is kept to ≤ 10 MeV on average.

In the reactions of channel (1), the kinetic energy carried by nucleons is a sizable fraction of the final-state hadronic energy. For reaction neutrons and for slow protons as well, most of this energy is not represented by ionizations produced in the scintillator tracker. In particular, secondary scatters of final-state neutrons occasionally give rise to localized ionization clusters—so-called neutron stars or “N-stars.” N-stars are usually observed at locations remote from primary vertices by factors of tens to hundreds of centimeters. Their energy depositions are much smaller than and are not proportional to the kinetic energy of the scattering neutrons released in antineutrino CC interactions [70]. Thus final-state N-stars in MINERvA contain insufficient information to enable neutron kinematic energy to be estimated on an event-by-event basis. Consequently this analysis intentionally avoids the use of nucleon-induced ionizations—neither neutron stars, nor hits within 10 cm of the primary vertex from slow protons—in its estimation of event-by-event $E_{\bar{\nu}}$. Instead, the analysis assembles all energies associated with reconstructed tracks and uses them as input for a kinematic estimation of $E_{\bar{\nu}}$ as described in Sec. V.

IV. SAMPLE SELECTION

Inclusion of events that have three reconstructed tracks ($\mu^+\pi^-$ plus proton) was initially considered. The number of 3-track events that pass the above-listed selections (excluding the 2-track topology requirement) is 110 events; the estimated signal purity of this subsample is 55%. Unfortunately, the presence of an additional track from the primary vertex gives rise to erroneous event reconstruction and introduces multipion background processes that are difficult to constrain. A full accounting of these aspects would introduce complications into the analysis while contributing little of added value. Consequently the selected sample of this analysis is, very

intentionally, restricted to two-track topologies, and the low-statistics 3-track subsample is excluded.

Cuts are imposed to ensure accurate interpretation of the event topology and to minimize background contamination. For the reconstructed pion, the start point is required to lie within 6 cm of the primary vertex. This selection ensures proximity to the vertex while allowing a single hit to be missed, as can happen with a track whose production angle exceeds 60° . Track reconstruction includes a fit-to-vertex step that ensures a degree of alignment. On the other hand, selected events must be devoid of “nonvertex tracks” whose initial hit is displaced radially by more than 6 cm from the vertex. Candidate events may have ionization hits that do not belong to the primary μ^+ and π^- tracks, provided that they are not part of a nonvertex track or of a “line segment”—the latter being a reconstructed cluster of hits that spans four or more contiguous planes. The π^- tracks of candidate events are required to stop in either the scintillator-tracking or ECAL regions of the central tracker. This requirement is needed to ensure that particle identification based on dE/dx and kinetic energy reconstruction based on range are done reliably. To this end, π^- endpoints are required to lie in a volume of hexagonal cross section surrounding the spectrometer's central axis. An apothem of 1 m is chosen so that all stopping points lie ≥ 15 cm inside the tracker's outer surfaces. Variation of this cut by ± 5 cm results in changes to differential cross sections that lie well within the statistical uncertainties.

The signal channel (1) involves the production of one and only one π^- meson. To eliminate backgrounds that give π^+ mesons, the regions surrounding primary vertices and around track endpoints are examined for occurrences of Michel electrons from decays of stopped π^+ tracks: $\pi^+ \rightarrow \mu^+ \rightarrow e^+$. Such decays give low-energy (≤ 100 MeV) EM showers that appear later than the candidate-event time by 0.5 to 16 μs . Events accompanied by a Michel-electron candidate are removed.

Figure 1 shows two data events from the candidate sample. Each interaction occurred in the central tracker and is displayed here in an X-view, looking down at the detector, using the Arachne event viewer [71]. The final-state muons traverse the scintillator planes of the tracker, ECAL, and HCAL regions and exit downstream. These muons give matches (spatially and in-time) to μ^+ tracks reconstructed in the magnetized MINOS detector. In each event the μ^+ is accompanied by a charged pion that ranges to stopping. The pions of the two events have kinetic energies of 118 MeV (upper panel) and 173 MeV (lower panel) and are fairly typical of pions in the candidate sample.

The event of the upper panel is devoid of extra hits around the vertex; the only ionizations are those on the muon and pion tracks. Candidate events may have additional hits arising, e.g., from inelastic scatters of π^- tracks or from isolated neutron hits. More interesting are

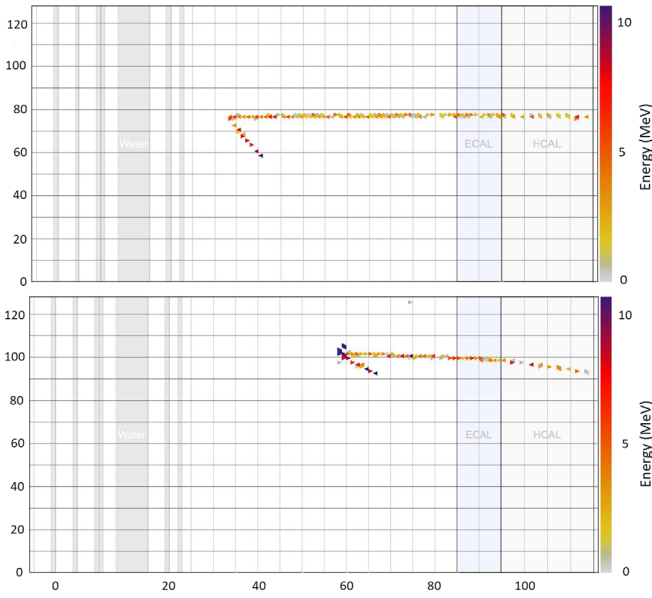


FIG. 1. Data candidates for signal channel (1). For each event, the $\bar{\nu}_\mu$ entered from the left and interacted within the central scintillator, yielding a μ^+ , a charged pion, originating from a primary vertex that is devoid of (upper panel) or else has (lower panel) additional ionization hits nearby. Horizontal and vertical axes show module and strip numbers, respectively. The right-side linear scale shows energy deposited in the strips.

additional hits in the vicinity of the vertex. Such an occurrence is illustrated by the event shown in the lower panel of Fig. 1. It has a pair of extra, heavily-ionized hits—a pattern that likely originates from a stopping proton. These two events indicate how distinctions based on extra energy at primary vertices can be used to statistically decompose the signal channel (1) into exclusive reactions, among which reactions (2) and (3) are major contributors. This line of inquiry is pursued in Sec. XII.

V. KINEMATIC VARIABLES AND FINAL SELECTIONS

As related above, p_μ is reconstructed using the muon's curvature and range in MINOS in conjunction with its dE/dx energy loss as it traverses the MINERvA tracker. The kinetic energy of the produced π^- , T_π , is assigned using track range. In traversing MINERvA's hydrocarbon medium however, negative pion tracks can undergo inelastic scattering or can be terminated by charge exchange or nuclear absorption; consequently track range tends to give an underestimate of true pion energy. To better estimate E_π of individual events, the calorimetric energy of ionization hits coincident with an event and in proximity to the π^- endpoint (see Sec. III) is added to T_π : $E_\pi = T_\pi + E_\pi^{\text{calo}}$. Then the initial direction of the π^- track, together with $|\vec{p}_\pi| = \sqrt{E_\pi^2 - m_\pi^2}$, establishes the pion 3-vector.

The incident antineutrino energy $E_{\bar{\nu}}$ is estimated on the basis of the kinematics of exclusive CC(π) reactions where

the struck nucleon is assumed to be at rest. Under this approximation, the incident antineutrino energy $E_{\bar{\nu}}$ is calculated according to the relation

$$E_{\bar{\nu}}^{\text{CC}(\pi)} = \frac{m_\mu^2 + m_\pi^2 - 2m_N E_b + E_b^2 - 2m_{N_b}(E_\mu + E_\pi) + 2\mathcal{P}_\mu \cdot \mathcal{P}_\pi}{2[E_\mu + E_\pi - |\vec{p}_\mu| \cos \theta_{\nu,\mu} - |\vec{p}_\pi| \cos \theta_{\nu,\pi} - m_{N_b}]}$$

Here, the 4-vector product in the numerator is $\mathcal{P}_\mu \cdot \mathcal{P}_\pi = E_\mu E_\pi - \vec{p}_\mu \cdot \vec{p}_\pi$, and m_{N_b} denotes the nucleon mass reduced by the binding energy, E_b , of the initial state nucleon: $m_{N_b} = (m_N - E_b)$. A value of 30 MeV is assigned to E_b based on electron scattering data [72,73].

The kinematic constraint for CC(π^-) channels utilized here is a modestly-refined version of the formula used previously by MiniBooNE in analysis of ν_μ -CC(π^+) scattering [74]. In essence, the formula accounts for invisible nucleon kinetic energy by requiring the vector momenta of final-state particles to balance with respect to directions transverse to the $\bar{\nu}_\mu$ beam.

With event $E_{\bar{\nu}} = E_{\bar{\nu}}^{\text{CC}(\pi)}$ determined as above, the nucleon T_N of each event (that is, the estimated kinetic energy of the interaction nucleon, neglecting Fermi motion and nuclear breakup contributions) can be inferred: $T_N = E_{\bar{\nu}} - (E_\mu + E_\pi + E_b)$. The shape of the data T_N spectrum obtained in this way peaks at 60 MeV and falls away approximately exponentially, reaching negligible rate by 1.0 GeV. Since the reference MC reproduces the derived spectral shape to within 17% over the full data range, it is reasonable to query the underlying simulation for some rough characterizations of neutron production: According to the MC, the average T_N per event is ~ 113 MeV for the selected sample. The average exhibits a linear correlation with incident $\bar{\nu}_\mu$ energy, varying from 75 MeV for $E_{\bar{\nu}}$ below 3 GeV, to 150 MeV for $E_{\bar{\nu}} = 9$ GeV. Final-state T_N is estimated to account for 2.9% of event $E_{\bar{\nu}}$ on average.

For $E_{\bar{\nu}}$ and for all other measured quantities in this work, the resolution is calculated as the r.m.s. width of the fractional residual error. The resolution for $E_{\bar{\nu}}$ is 9.5%. With event-by-event estimations of $E_{\bar{\nu}}$ in hand, the four-momentum-transfer squared, Q^2 , and the hadronic invariant mass, W , are then calculated as follows:

$$Q^2 = -(k - k')^2 = 2E_{\bar{\nu}}(E_\mu - |\vec{p}_\mu| \cos \theta_\mu) - m_\mu^2, \quad (5)$$

and

$$W^2 = (p + q)^2 = m_N^2 + 2m_N(E_{\bar{\nu}} - E_\mu) - Q^2. \quad (6)$$

Here, k , k' , and p are the four-momenta of the incident neutrino, the outgoing muon, and the struck nucleon respectively, while $q = k - k'$ is the four-momentum transfer and m_N is the nucleon mass.

The resolution for the variable Q^2 is 0.09 GeV^2 . Concerning the hadronic mass W , the formula of Eq. (6) is based on the assumption that the struck nucleon is initially at rest. It is therefore useful to distinguish between the estimator W_{exp} used by this analysis vs the “true W ” of the reference simulation. The analysis estimates the hadronic mass, W_{exp} , of each signal event using Eq. (6). The resolution in W_{exp} for this analysis is 0.12 GeV (0.17 GeV) for $W_{\text{exp}} < 1.4 \text{ GeV}$ ($W_{\text{exp}} > 1.4 \text{ GeV}$).

As final selections for the signal sample, reconstructed neutrino energies of selected events are restricted to the range $1.5 \text{ GeV} < E_{\bar{\nu}} < 10 \text{ GeV}$ and an upper bound of 1.8 GeV is placed on W_{exp} . The lower bound on $E_{\bar{\nu}}$, together with the upper bound on θ_{μ} (see Sec. III), ensures good acceptance for muons to be matched in MINOS, and the upper bound on W_{exp} mitigates background from CC multi-pion production. In summary, three kinematic selections comprise the signal definition of this analysis: (i) $\theta_{\mu} < 25^\circ$ for the μ^+ track at production, (ii) $1.5 < E_{\bar{\nu}} < 10.0 \text{ GeV}$ for the antineutrino energy, and (iii) $W_{\text{exp}} < 1.8 \text{ GeV}$ for the hadronic invariant mass.

The analysis signal sample after all selections contains 1606 data events. The average selection efficiency is the ratio of selected signal events to total signal events. This efficiency, as estimated by the simulation, is 5.8%. The sample purity, defined as the number of signal events divided by the number of selected events, is also estimated using the MC. The purity is 72%, implying that approximately 1156 of selected data events are actual occurrences of channel (1). The average energy of the $\bar{\nu}_{\mu}$ flux over the analyzed $E_{\bar{\nu}}$ range is 3.5 GeV, while the average $E_{\bar{\nu}}$ for the selected signal sample is 3.76 GeV. That the latter average exceeds the former reflects the rise in the signal channel cross section with increasing $E_{\bar{\nu}}$ (see Sec. XI).

Figure 2 presents initial comparisons of the selected signal sample to reference MC predictions using distributions, prior to background subtraction, of directly-measured kinematic variables for final-state μ^+ and π^- mesons (upper, lower plots respectively). The error bands associated with the MC histograms include uncertainties associated with GENIE modeling of both signal and background processes including non-resonant pion production as described in Sec. II B. The simulation histograms give respectable descriptions of the shapes of the data distributions. For absolute event rates, however, there is a data-MC offset, with the MC prediction lying above the data in most bins. This excess rate predicted by the MC represents an 10% increase in total event rate compared to the data. (This initial excess is reduced to 8% by the background constraint of Sec. VI.) Nevertheless, the data points are mostly contained by the $\pm 1\sigma$ systematic error band of the MC prediction. The selected signal sample includes background events, mostly comprised of CC scattering into single-pion or two-pion final states that differ from channel (1). Their contribution is estimated by the reference MC and is shown by the

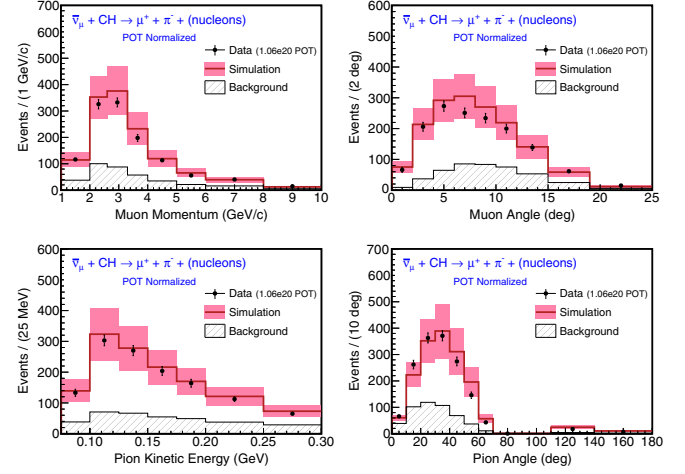


FIG. 2. Initial data distributions of the selected sample for μ^+ and π^- kinematic variables p_{μ} , θ_{μ} (upper plots) and T_{π} , θ_{π} (lower plots) compared to the reference MC predictions (histograms with systematic error band). The comparisons here are shown before constraining the background (lowermost gray-shade histogram) via sideband fitting, and prior to correcting the data for detector effects.

gray-shade component histograms of Fig. 2. The overall good agreement between the data and the reference simulation at this stage is sufficient to justify its utilization by the analysis to estimate detection efficiencies and to make corrections for detector response.

VI. BACKGROUND CONSTRAINT FROM SIDEBAND FITTING

The signal sample includes background processes whose final-state particle content upon exit from the target nucleus is inconsistent with channel (1). While the reference MC provides estimates for the rate and kinematic behavior of background events, these estimates come with large uncertainties. Fortunately, the estimation of background can be greatly constrained by tuning the reference MC to well-describe a background-rich “sideband sample” whose events have topological and kinematic resemblances to the selected signal events. A search for a useful sideband was carried out by inspecting samples obtained by turning off just one selection cut from the ensemble that defines the signal sample. Within the full set of cuts there are four specific ones that, when individually reversed, allow a useful sideband subsample to be defined. Then, by collecting events that pass all signal selections but one, wherein the sole rejection arises with one of the four specific cuts, a single sideband sample with discriminatory power and good statistics is obtained.

The four selection cuts are: (i) no reconstructed remote tracks are allowed in the event, (ii) all reconstructed line segments must belong to the μ^+ or π^- tracks, (iii) the leading hit of the pion track must lie within 6 cm of the vertex, and (iv) the event cannot have a Michel electron.

Each data event of the sideband satisfies all signal selections but one, with the excepted selection being one of the four above-listed cuts. The sideband sample, assembled in this way, contains 4887 events.

The reference MC is amenable to a simple tuning fit to the sideband; this situation was discerned by comparing the MC predictions to data distributions of the sideband sample using the kinematic variables measured by the analysis. These include the directly measured variables of μ^+ momentum and production angle (p_μ and θ_μ), pion kinetic energy and production angle (T_π and θ_π), and the derivative variables $E_{\bar{\nu}}$, Q^2 , and W_{exp} . The reference MC was found to describe the shapes of all seven distributions fairly well, while the absolute rate prediction was higher by $\sim 2\%$.

The initial comparison of the MC with sideband data is displayed in Fig. 3 which shows the sideband distributions for the kinematic variables of the μ^+ and π^- tracks. The prediction of the reference MC prior to tuning (histograms) exceeds the sideband data in the majority of bins. Approximately 75% of the sideband consists of background (lower histograms), originating mostly from CC RES or nonresonant DIS interaction categories that give rise to multipion final states. Importantly, the remaining $\sim 25\%$ of background is estimated to be “signal contamination” as shown by the upper component histograms in Fig. 3. This component of the sideband arises with events that fail the selection criteria as the result of shortfalls in event reconstruction. Clearly, the presence of signal events in the sideband must be accounted for when fitting the reference MC to match the sideband distributions. That said, it is possible to tune the reference MC to

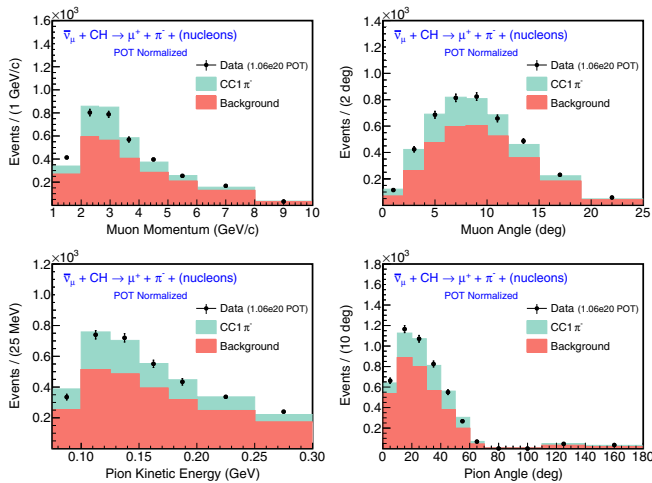


FIG. 3. Muon and charged pion kinematic distributions for sideband data events (solid points with statistical error bars) compared to the reference simulation (histograms) prior to tuning. The MC describes the shape but slightly overestimates the rate of sideband data. Lower-component histograms (red) show the estimated background content of the sideband. Upper-component histograms (green) depict the signal contamination in the sideband.

match the sideband data distributions for all seven of the above-listed variables using the iterative procedure described below.

For sideband distributions in each of p_μ , θ_μ , T_π , θ_π , $E_{\bar{\nu}}$, Q^2 , and W_{exp} , the distribution shapes for true background and for signal contamination are taken from the MC prediction while the absolute rate normalizations for these two components are treated as parameters in a χ^2 fit. Fitting of the MC prediction to the sideband distributions proceeds in two steps, and these are subsequently iterated. In the first step, the background normalization for the MC (a single parameter) is allowed to vary in a fit to the seven kinematic distributions of the sideband data, while the signal contamination normalization is held fixed. In the second step, a similar simultaneous fit to the kinematic distributions of the signal sample is carried out, but with the MC background estimate fixed according to the outcome of step one, while the normalization of the predicted signal content serves as the fit parameter. The revised normalizations for MC-estimated signal and background then serve as input for another two-step fitting sequence. This two-step fitting of sideband and then signal samples is repeated until the background and signal normalizations settle onto stable values. This fitting procedure converges with four iterations.

At this stage the simulation vs data was examined in each bin of the sideband distributions for all seven kinematic variable (62 bins) and the verity of predicted rate and shape was evaluated. Good agreement was observed overall. The sole exception was with three contiguous bins spanning the peak of the sideband W_{exp} distribution wherein the MC prediction was $1.2 - 2.5\sigma$ higher than the data. This mild discrepancy is attributed to background events in the simulation, and weights (averaging 0.88) are assigned to MC events in the three W bins to bring the simulation closer to the data. Incorporation of these weights gives small adjustments ($\leq 2\%$) to background estimates in bins of the other kinematic variables. An uncertainty of 100% is assigned to the weights and is propagated to the final error budget.

The result of iteratively fitting the background plus signal normalizations and tuning the predicted background W_{exp} shape is summarized in Figs. 4, 5, and 7. Figure 4 shows the sideband distributions of the directly measured muon and pion kinematic variables prior to any adjustment. The reference MC reproduces the distribution shapes quite well, with small discrepancies in absolute rate discernible in a few bins. The MC predictions, however, have significant flux and GENIE modeling uncertainties associated with them, as indicated by the shaded error bands. The sideband distributions for these same directly-measured variables after fitting and tuning, together with the derivative variables $E_{\bar{\nu}}$ and Q^2 , are shown in Fig. 5. Here, the match between data points and MC histograms is changed slightly by the fitting and tuning procedure. The main effect is that the fit constrains uncertainties associated with

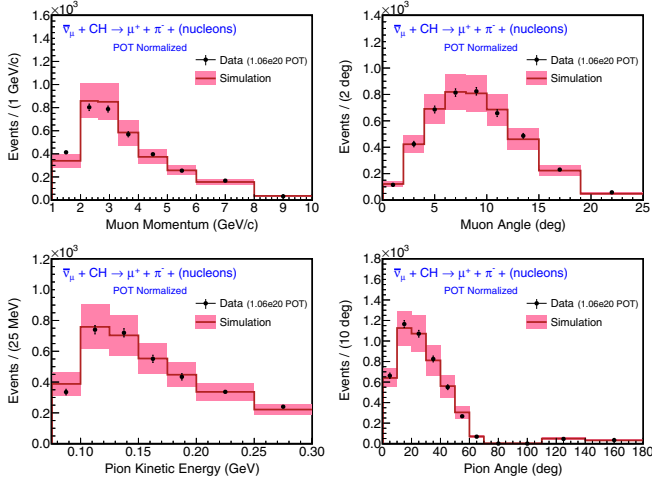


FIG. 4. Sideband sample distributions, MC vs data, for muon and pion kinematic variables (upper, lower plots respectively) prior to tuning of background and signal-contamination normalizations. The initial MC predictions and total systematic uncertainties are shown by the histograms and shaded error bands.

event-rate prediction and thus reduces the error bands of the tuned MC prediction.

Figure 6 shows the sideband distribution of the variable least directly measured, namely W_{exp} , before and after

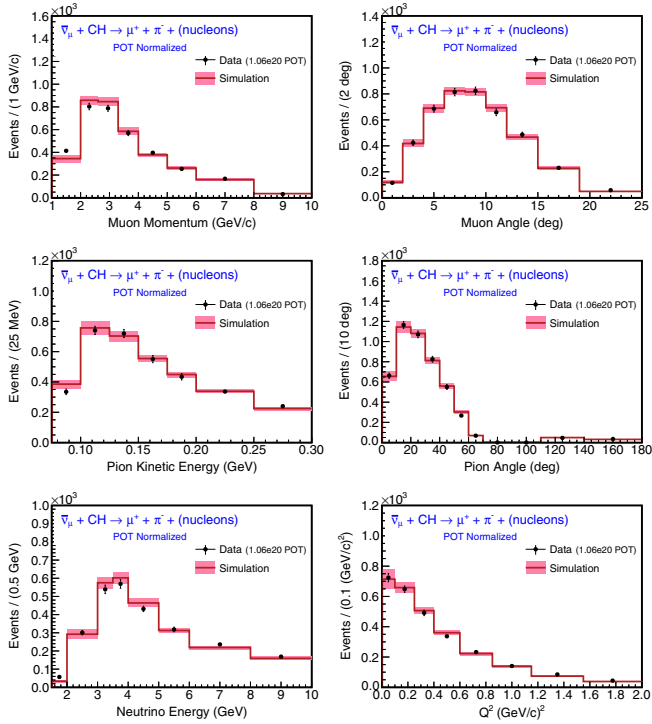


FIG. 5. Sideband distributions, MC vs data, for muon and pion variables as in Fig. 4, plus distributions for $E_{\bar{\nu}}$ and Q^2 . The MC predictions (histograms with error bands) are shown after the iterative fit of background and signal normalizations to seven kinematic distributions of the sideband and signal samples, and weight-adjusting the MC in 3 bins of W_{exp} . (see main text).

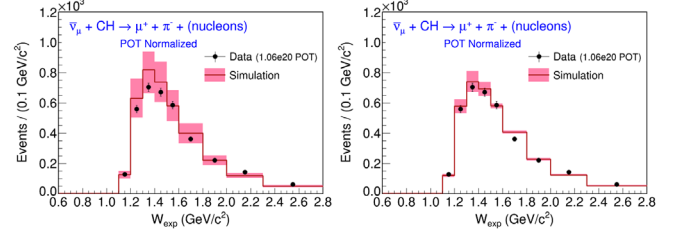


FIG. 6. Sideband distributions, MC vs data, for estimated hadronic mass W_{exp} . Left-side plot shows sideband W_{exp} prior to any adjustment of the MC. Right-side plot the improved agreement of MC (histogram with error bands) with the data after fitting of normalizations and weighting of the MC rate through the peak ($1.2 < W_{\text{exp}} < 1.5$ GeV).

fitting and tuning. The initial MC overprediction through the peak region $1.2 < W_{\text{exp}} < 1.5$ GeV, discernible in Fig. 6 (left), is weight-adjusted to give the improved agreement shown in Fig. 6 (right). The net change to the background normalization from the iterative fit plus shape tuning is an increase of +1%. The fit also imposes a 11% reduction in the estimated signal contamination in the sidebands.

After tuning the background estimate using the sideband distributions as above, the reference MC is used to predict the background contribution, N_j^{bkg} , for the j th bin of any specific distribution of signal-sample events. The true signal content is then calculated as $(N_j^{\text{data}} - N_j^{\text{bkg}})$, where N_j^{data} is the number of data candidates.

VII. DETERMINATION OF CROSS SECTIONS

Calculation of the flux-integrated differential cross section per nucleon for kinematic variable X (such as p_{μ} , θ_{μ} , and Q^2), in bins of i , proceeds as follows [10–13]:

$$\left(\frac{d\sigma}{dX}\right)_i = \frac{1}{\mathcal{T}_N \Phi} \frac{1}{\Delta X_i} \frac{1}{\epsilon_i} \sum_j M_{ij} (N_j^{\text{data}} - N_j^{\text{bkg}}), \quad (7)$$

where \mathcal{T}_N is the number of target nucleons in the fiducial volume, Φ is the integrated flux, ΔX_i is the bin width, ϵ_i is the selection efficiency and acceptance. The matrix M_{ij} is the unfolding matrix [75]. It calculates the contribution to true bin i from reconstructed bin j , where the j th bin contains N_j^{data} number of data candidates and N_j^{bkg} number of background events. Calculation of $\sigma(E_{\bar{\nu}})_i$, the cross section per antineutrino energy bin i , is carried out using an expression that can be obtained from Eq. (7) by dropping ΔX_i and changing Φ to Φ_i , the $\bar{\nu}_{\mu}$ flux for the i th bin of $E_{\bar{\nu}}$.

The background-subtracted data is subjected to iterative unfolding [75]. The unfolding procedure takes detector resolution smearing into account and corrects reconstructed values (j) to true values (i) according to mappings, M_{ij} , determined by the reference simulation. For most of the

kinematic variables measured in this work, the unfolding matrices are close to diagonal and the effects of unfolding are minor. Differences between unfolded distributions diminish rapidly with consecutive iterations and convergence was achieved within 3 iterations for p_μ , θ_μ , θ_π , and within 5 iterations for $E_{\bar{\nu}}$ and Q^2 .

Final estimation of π^- kinetic energy is an exceptional case; here the unfolding procedure introduces a significant, necessary correction. With T_π , visible track range is used to assign an initial value and it tends to give an underestimate. This is because the T_π of a negative pion, initially produced with several-tens to few-hundreds MeV, is swept through the $\Delta(1232)$ excitation region as the pion ranges out. Consequently scattering occurs at elevated rates in modes that terminate tracks (via charge exchange or absorption) and/or drain away energy via inelastic transfer to unbinding, recoiling nucleons. Track ranges thereby tend to be abbreviated, with T_π being somewhat underestimated. Consequently the unfolding procedure requires a relatively large number of iterations in order to converge to a final result. The differential cross section $d\sigma/dT_{\pi^-}$ reported in this work (see Sec. X) is obtained using ten unfolding iterations.

For all of the above-mentioned kinematic variables including T_π , the stability of unfolded solutions was checked by unfolding ensembles of MC samples representing perturbed variations of the initial data distributions.

The bin-by-bin efficiency ϵ_i is estimated using the simulation. The selection efficiency vs muon momentum, for example, rises from 4% below 2 GeV/c and climbs to 9% at 4.0 GeV/c, as the result of improved μ^+ tracking acceptance ($\theta_\mu < 25^\circ$) for higher-momentum μ^+ tracks in the MINOS near detector. Above 6 GeV, the efficiency gradually diminishes as the result of the $E_{\bar{\nu}}$ cut at 10 GeV. As previously stated, the overall selection efficiency for signal events is 5.8%.

The analysis uses current determinations of the integrated and differential $\bar{\nu}_\mu$ fluxes over the $E_{\bar{\nu}}$ range 1.5 to 10 GeV for the NuMI low-energy antineutrino beam mode [40]. The $\bar{\nu}_\mu$ flux in bins of $E_{\bar{\nu}}$ is given in the Supplemental Material [76]. The value for the integrated flux Φ is $2.00 \times 10^{-8} \bar{\nu}_\mu/\text{cm}^2/\text{POT}$.

VIII. SYSTEMATIC UNCERTAINTIES

Cross section measurements require knowledge of selection efficiencies, detector acceptance and resolutions, distribution shapes and normalizations of backgrounds, and the antineutrino flux. The estimation of each of these quantities introduces uncertainties. Many of the sources of uncertainty that affect the present work were encountered by previous MINERvA studies of CC(π) interactions and their treatment has been described in publications [10–13]. The systematic uncertainty from the antineutrino flux is described in detail in Refs. [40,77].

The sources of uncertainty can be grouped into six general categories. In Figs. 7 and 8 of this section, and in tables of the Supplemental Material [76], the fractional uncertainties for each bin of each measurement are decomposed using these categories. The first category, designated by “Detector,” is assigned to detector response uncertainties arising from particle energy scales, particle tracking and detector composition. Categories two, three, and four include, respectively, uncertainties from simulation modeling of neutrino interactions, GENIE model uncertainties for FSI involving produced hadrons, and antineutrino flux uncertainties. These categories are designated as “X-Sec Model”, “FSI Model”, and “Flux”. Then there are uncertainties that arise with estimation of rate and distribution shapes for the background; these are compiled in the category labeled “Bkg Est.” Finally, there are statistical uncertainties that reflect finite sample sizes and the

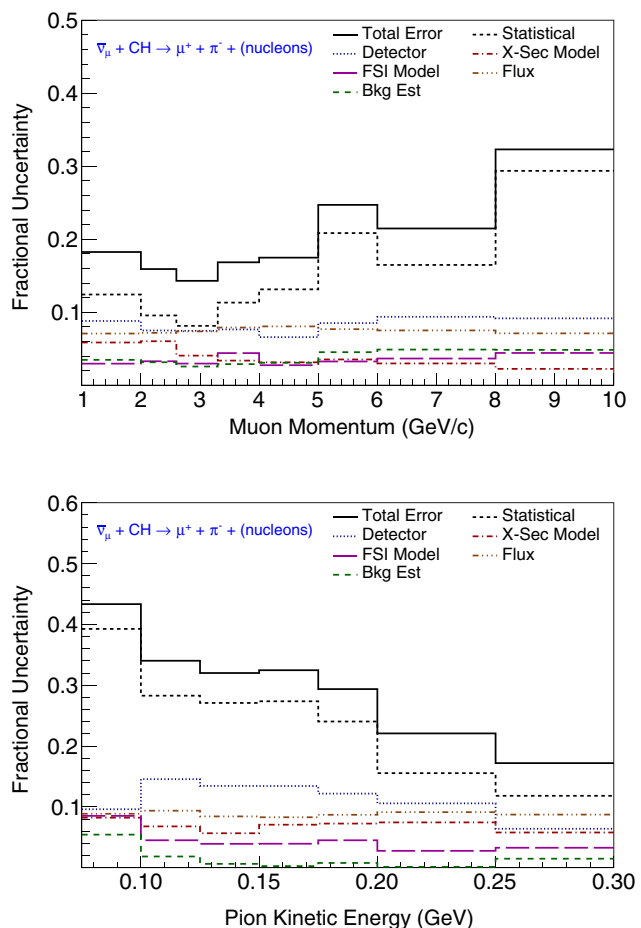


FIG. 7. Composition of fractional uncertainty in terms of systematic error categories plus the statistical uncertainty, for differential cross sections in μ^+ momentum (upper plot) and π^- kinetic energy (lower plot). The statistical uncertainty (short-dash-line histogram) is the leading error source in all bins, with detector response (fine-dash) and antineutrino flux (dot-dot-dash) uncertainties also contributing significantly.

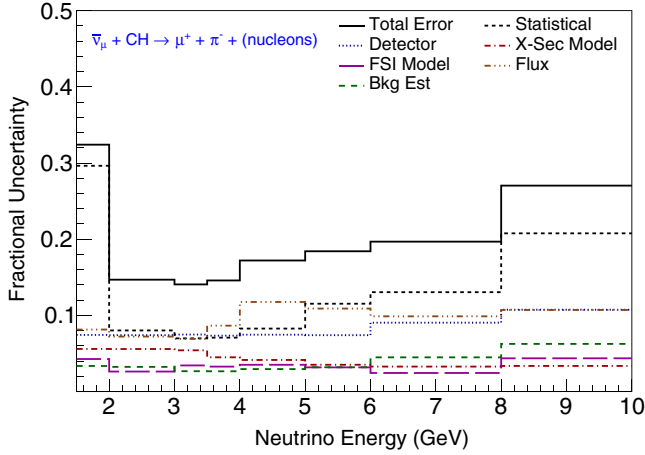


FIG. 8. Bin-by-bin fractional uncertainty in systematic error categories plus statistical uncertainty, for cross section as a function of $E_{\bar{\nu}}$. The flux and detector response uncertainties are comparable to the statistical uncertainty in the 2.0 to 6.0 GeV range of $E_{\bar{\nu}}$.

consequent uncertainties that these generate in the unfolding. These are included together in the “Statistical” category.

Systematic uncertainties are evaluated by shifting the relevant parameters in the simulation about nominal values within their $\pm 1\sigma$ bands and producing a new simulated event sample. Cross sections are then recalculated using an ensemble of such alternate-reality samples, and a covariance matrix is formed from the results. The procedure is repeated for each systematic source; details are given in Ref. [12]. On cross section plots to follow, the error bars shown represent the square roots of covariance diagonal entries. The full correlation matrices are given in the Supplemental Material [76].

Uncertainty decompositions representative of cross-section determinations of directly measured kinematic variables are shown in Fig. 7, for μ^+ momentum (upper plot) and for charged pion kinetic energy (lower plot). For all bins of either distribution, the finite data statistics (short-dash histogram) gives rise to larger uncertainties than does any single systematic category. In particular, the large statistical error assigned to pion kinetic energies below 200 MeV reflects a large unfolding-correction uncertainty. The detector response category contributes fractional uncertainties that range from 7% to 9% for muon momentum, and from 6% to 15% for pion kinetic energy. Uncertainties assigned to the antineutrino flux are subject to constraints provided by the background normalization procedure. Figure 7 shows the fractional uncertainties from the flux and from the interaction cross section model (GENIE) categories to be constant or slowly varying over the measured ranges of p_{μ} and T_{π} , with value ranges of 7% to 8% and 8% to $\leq 10\%$ respectively.

The differential cross sections of this work include $E_{\bar{\nu}}$ and Q^2 . Since these variables are less directly related to

observations than are the muon and pion, their uncertainties have compositions that differ somewhat from those shown in Fig. 7. By way of illustration, the uncertainty decomposition for $E_{\bar{\nu}}$ is shown in Fig. 8. Here the statistical uncertainty dominates the low (< 2.0 GeV) and high (> 6.0 GeV) neutrino energy bins, however in the $E_{\bar{\nu}}$ range central to this work the flux and detector response give fractional uncertainties of 9%–12% and 9% respectively—values that rival or exceed the statistical error.

The six uncertainty categories encompass all significant systematics of the analysis, including the methodology by which nucleon kinetic energy is treated. Nevertheless, it is of interest to quantify the sensitivity of the $E_{\bar{\nu}}$ determination to the reliance on kinematics for the inclusion of final-state nucleon T_N . For this purpose a simulation study was performed wherein an uncertainty band for T_N was assigned that covers the difference between binned values extracted by the analysis vs MC true values. Fractional uncertainties of 5%, 10%, and 25% were allotted to T_N ranges of 0–125 MeV, 125–200 MeV, and > 200 MeV respectively. Simulation data for T_N was then varied randomly in accord with the error band and $E_{\bar{\nu}}$ was recalculated. The resulting r.m.s. spread in the fractional deviation of $E_{\bar{\nu}}$ was less than 2.0% overall, with deviations trending to higher values for $E_{\bar{\nu}} > 5.5$ GeV. As Fig. 8 clearly shows, an uncertainty of this magnitude is well-covered by the ensemble of systematic and statistical uncertainties assigned to the $E_{\bar{\nu}}$ measurement.

IX. MUON KINEMATICS OF $\bar{\nu}_{\mu}$ -CC(π^-)

A. Muon momentum

Figure 9 shows the differential cross section for μ^+ momentum, $d\sigma/dp_{\mu}$, of the signal channel. The data are shown by the solid circles in the figure, with fully (partially) extended error bars denoting the total (statistical) error associated with each data point. Included in the cross section is a small event rate from CC coherent scattering reaction (4) whose estimated contribution is indicated by the shaded area along the base of the distribution. In accordance with the analysis signal definition, this differential cross section (and all others to follow) is flux-integrated over the range $1.5 \text{ GeV} \leq E_{\bar{\nu}} \leq 10 \text{ GeV}$, with the μ^+ direction at production restricted to $\theta_{\mu} \leq 25^\circ$. The $\bar{\nu}_{\mu}$ flux spectrum strongly influences the shape of $d\sigma/dp_{\mu}$. The distribution peaks near 2.5 GeV and then falls off rapidly as p_{μ} increases. Predictions obtained with the GENIE-based MC are shown by the two upper-most (red) curves in Fig. 9. The dashed curve depicts a simulation in which pion and nucleon FSI effects are neglected. It differs significantly from the full reference simulation with FSI included, shown by the solid-line curve. The difference is an average event-rate reduction of nearly 20%, reflecting the strength of pion FSI in carbon, principally with π^- absorption, for pions produced with kinetic energies in the region of $\Delta(1232)$

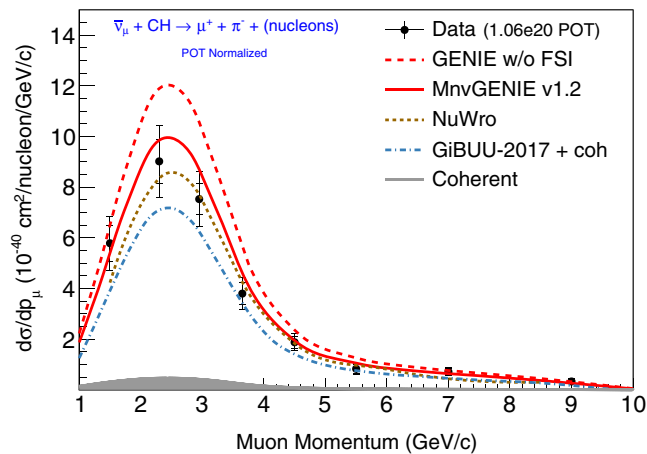


FIG. 9. The flux-integrated muon-momentum differential cross section, $d\sigma/dp_\mu$ for muons with $\theta_\mu \leq 25^\circ$. Data (solid circles) are shown with inner (outer) error bars that denote the statistical (total) uncertainties. The solid-line (dashed) curves show GENIE predictions with (without) FSI. Short-dash and dot-dash curves show predictions by NuWro and GiBUU-2017. The estimated contribution from CC coherent scattering (4) is given by the shaded region.

excitation by π^- intranuclear scattering. With inclusion of FSI, the GENIE-based simulation still lies above the data, giving an absolute event rate that exceeds the data by 8%. Allowing for the overestimate, one sees that the shape of the distribution is approximately reproduced for $p_\mu > 2$ GeV/c.

The short-dash and dot-dash curves in Fig. 9 that lie below the GENIE prediction show expectations based on the NuWro and GiBUU-2017 event generators respectively. NuWro does better than either GENIE or GiBUU-2017 with predicting the absolute data rate for most of the momentum range, with exception of momenta below 2 GeV/c where GENIE matches the observed rate while the NuWro and GiBUU-2017 predictions fall below the data. When each of the three generator predictions for this differential cross section is area-normalized to the data (not shown), the generator curves nearly coincide and all three generators give a good characterization of the distribution shape.

The events of signal channel (1) can be characterized as originating from one of four processes: (i) pion production via the $\Delta(1232)$ resonance, (ii) pion production via other baryon resonances, (iii) Non-resonant pion production including DIS reactions, and (iv) coherent pion production via reaction (4). Figure 10 shows the relative strengths of these processes as predicted by the reference simulation. According to GENIE, Δ^- production accounts for 59% of the rate (upper, light-shade histogram in Fig. 10); production and decay of higher-mass N^* resonances gives an additional $\simeq 20\%$, with nonresonant pion production and CC coherent scattering accounting for the remaining 17% and 4% of the total rate, respectively. These rates are for final states at emergence from target nuclei, having been

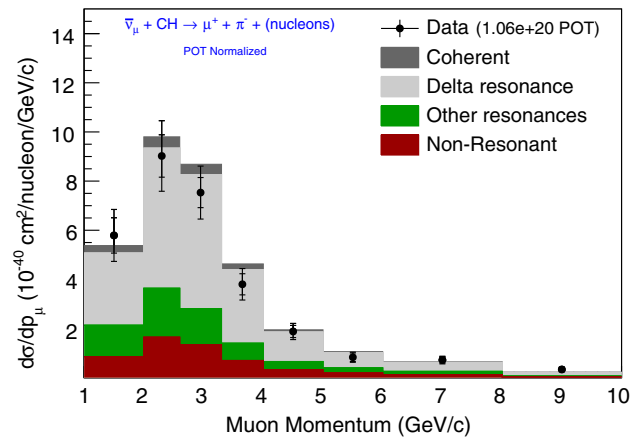


FIG. 10. Cross section $d\sigma/dp_\mu$ as in Fig. 9, compared to component reaction processes of the reference simulation. Production of $\Delta(1232)^-$ is predicted to dominate the signal channel (gray-shade histogram) in all bins of muon momentum.

subjected to hadronic intranuclear scattering. Their relationship to initially produced final states is inferred using the FSI model of the reference MC. The relationship is well-illustrated by CC nonresonant single- π^- events wherein 12.5%, 9.5%, and 1.6% portions of the initial sample migrate out of channel (1) as the result of pion absorption, pion charge exchange, and of other hadronic FSI.

The four processes listed above are broadly distributed within the muon momentum distribution. Figure 10 indicates that the rate mismatch between GENIE and data could be alleviated by reducing contribution(s) from the three noncoherent processes, but the data do not allow a unique prescription to be identified.

B. Muon production angle

Figure 11 shows the μ^+ differential cross section as a function of polar angle, θ_μ , with respect to the beam direction. The distribution peaks near 7° and then decreases gradually at larger angles.

Comparison of GENIE, NuWro, and GiBUU-2017 predictions to the data show similar trends to those noted in Fig. 9. All three generators give fairly accurate characterizations of the shape of $d\sigma/d\theta_\mu$, although the data above $\sim 6^\circ$ exhibits a relatively flatter distribution. Readily discernible is the overprediction of absolute rate by GENIE and its underprediction by GiBUU-2017, with the closest agreement being achieved by NuWro. The small contribution expected from CC coherent single-pion production (shaded region in Fig. 11) is mostly confined to θ_μ into forward angles $< 10^\circ$. The fractional contributions from the three most prominent processes displayed in Fig. 10 are predicted by GENIE to be nearly uniformly distributed over the measured angular range.

The cross sections $d\sigma/dp_\mu$ and $d\sigma/d\theta_\mu$ can be compared to those previously reported by MINERvA for $\bar{\nu}_\mu$ -CC($1\pi^0$)

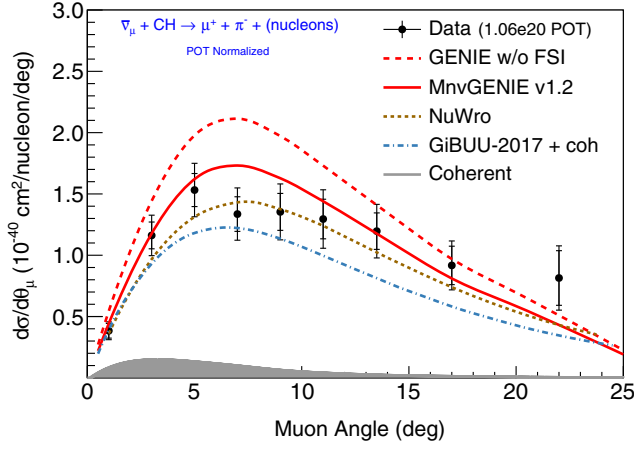


FIG. 11. Differential cross section for muon production angle, $d\sigma/d\theta_\mu$. Data (solid circles) is compared to the predictions of GENIE with and without FSI (dashed, solid uppermost curves) and with predictions from NuWro and GiBUU-2017. The distribution shape is reproduced by all generators; NuWro comes closest with predicting the absolute event rate.

and for ν_μ -CC(π^+) and ν_μ -CC($1\pi^0$) [11,13]. The observed spectral peaks roughly coincide for all four data sets, even though the absolute cross sections are fairly different. Differences in cross section magnitudes are certainly to be expected, since the four pion production channels differ in their isospin compositions and in the role played by interferences between vector current and axial vector current contributions, the latter being constructive in the ν_μ channels and destructive in the $\bar{\nu}_\mu$ channels.

X. PION KINEMATICS OF $\bar{\nu}_\mu$ -CC(π^-)

Figure 12 shows the differential cross section for pion kinetic energy, $d\sigma/dT_{\pi^-}$. Events in the lowest T_{π^-} bin have short π^- tracks and their detection efficiency (2.8%) is 2.4 times lower than that of the next higher bin. The efficiency correction to this bin mostly removes the depletion that appears in the initial data distribution for pion kinetic energy (lower-left plot of Fig. 2). Additionally, the efficiency correction tends to flatten the remainder of the distribution. The bin-by-bin uncertainties assigned to the data points are relatively large, reflecting the fact that the kinetic energy estimation for π^- tracks receives sizable corrections from the unfolding procedure. The upper plot shows the gradually-falling shape of $d\sigma/dT_{\pi^-}$ to be reproduced by predictions from the generators, and the absolute rate is roughly described. The level of agreement provides support for the various FSI treatments for pions initiated within carbon nuclei that are invoked by GENIE, NuWro, and GiBUU.

Produced π^- mesons of the signal channel and the pions of background reactions as well can undergo absorption, elastic and inelastic scattering, and/or charge exchange as they traverse the struck nucleus. These pion FSI processes

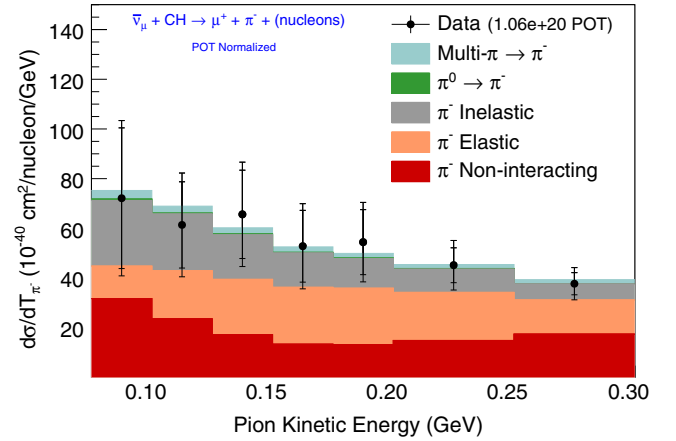
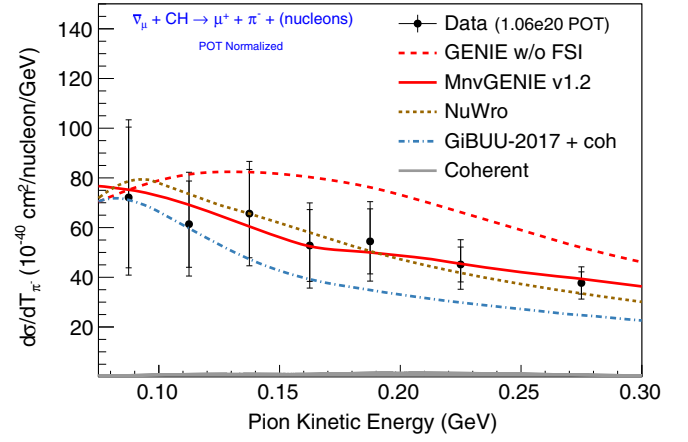


FIG. 12. Differential cross section $d\sigma/dT_{\pi^-}$ for pion kinetic energy. Upper plot compares the data (solid points) to predictions by the GENIE-based MC, NuWro, and GiBUU-2017. Lower plot shows that GENIE achieves agreement with measured $d\sigma/dT_{\pi^-}$ by combining pion FSI processes that differ in their component shapes.

are especially prominent in range $90 \text{ MeV} < T_\pi < 210 \text{ MeV}$ corresponding excitation of the Δ in π^- scattering on carbon [78]. The agreement obtained by the GENIE-based MC for $d\sigma/dT_{\pi^-}$ is notable because the prediction represents a fairly intricate prediction that involves all pion subprocesses of the FSI model.

A breakdown of contributions from the component processes is presented in the lower plot of Fig. 12. The stacked histograms indicate that pions experiencing inelastic scattering, elastic scattering, or no scattering comprise the bulk of the sample (three lowest histograms), while background feed-in from multiple-pion production with absorption and from $\pi^0 \rightarrow \pi^-$ charge exchange occurs with small rates (two uppermost histograms). These processes are in addition to the significant amounts of absorption and charge-exchange that π^- from initially produced signal events are predicted to undergo. According to the GENIE model, these latter processes have already winnowed down the signal sample from the initial interaction rate shown by

the GENIE prediction without FSI (dashed curve in upper plot of Fig. 12), to give the rate predicted with FSI included—depicted by the solid curve (upper plot) and the summed histograms (lower plot) of Fig. 12. Thus reproduction of the observed π^- kinetic energy is achieved in the GENIE model by accounting for the combined effect of pion intranuclear elastic and inelastic scattering, charge exchange, absorption, together with instances of free pion propagation through target carbon nuclei.

Figure 13 shows the differential cross section in pion angle measured relative to the $\bar{\nu}$ beam direction. The data shows that most π^- s are produced in the forward hemisphere of the Lab frame, with angles around 30° being most probable. The upper plot shows that the regions on either side of the peak are not well described by the event generators. The data includes occurrences of CC coherent

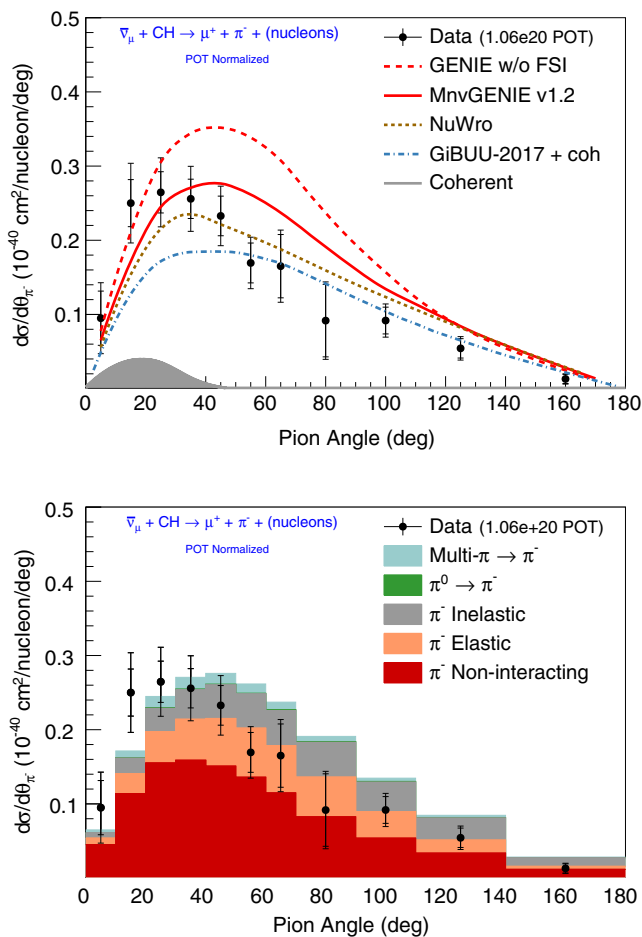


FIG. 13. Differential cross section for pion production angle. Upper plot shows the data with predictions from the GENIE-based MC and from NuWro and GiBUU-2017. The gray-fill distribution depicts CC coherent scattering as measured by MINERvA. Although coherent scattering is included in all the generator predictions, the data rate into forward $<20^\circ$ is under-predicted. Lower plot shows contributions to $d\sigma/d\theta_{\pi^-}$ from component pion FSI processes as estimated by the GENIE MC. Coherent scattering is included in “ π^- noninteracting.”

scattering via reaction (4), and this reaction is included in all of the generator predictions displayed in the figure. In particular, the CC coherent contribution measured by MINERvA is shown by the gray-fill distribution in the upper plot. This contribution is included in the GENIE-based reference simulation shown by the solid curve in the upper plot. It is also included as part of the “ π^- non-interacting” component displayed in the lower plot. In the upper plot, the χ^2 per degrees of freedom for the reference simulation with (without) FSI is 24.2/11(47.8/11), while for NuWro and GiBUU-2017 it is 15.3/11 and 12.7/11, respectively.

The lower plot in Fig. 13 decomposes the GENIE prediction into pion FSI processes, with “pion noninteracting” (plus coherently produced) being included as a process. None of the component processes are predicted to have angular features that change rapidly with increasing θ_{π^-} . Modeling of the inelastic and elastic FSI contributions include prescriptions for deflections of the initial pion direction. Presumably these could be adjusted to give a better description of the data.

XI. CROSS SECTIONS FOR $E_{\bar{\nu}}$ AND Q^2

Figure 14 shows the cross section as function of antineutrino energy, $\sigma(E_{\bar{\nu}})$, for the signal sample, for which the invariant hadronic mass is restricted to $W_{\text{exp}} < 1.8$ GeV. The data exhibit a gradual rise from threshold that continues with increasing $E_{\bar{\nu}}$ to the end of the measured range at 10 GeV. This behavior contrasts with the cross-section energy dependence of ν_μ -induced $\text{CC}(\pi)$ wherein the slope of $\sigma(E_{\bar{\nu}})$ turns over and remains nearly zero above ~ 5 GeV [11,13]. These differing trends reflect the underlying vector minus axial vector ($V - A$) structure of the hadronic current in $\Delta S = 0$ semileptonic interactions. The VA interference terms contribute significantly to the cross sections at sub-GeV to few-GeV values of $E_{\bar{\nu}}$, however they diminish rapidly relative to the $|V|^2$ and $|A|^2$ terms at higher incident (anti) neutrino energies. In contrast to ν_μ -induced $\text{CC}(\pi)$ cross sections, VA interference terms are of opposite sign and destructive for $\bar{\nu}_\mu$ - $\text{CC}(\pi)$ interactions. Consequently the slope turn-over point for cross sections of antineutrino $\text{CC}(\pi)$ channels occurs at a distinctly higher incident energy than is observed with neutrino-induced $\text{CC}(\pi)$.

The three curves representing predictions based on GENIE, NuWro, and GiBUU-2017 in Fig. 14 (upper plot) exhibit the expected gradual rise of the cross section with $E_{\bar{\nu}}$. The GENIE-based reference MC is in agreement with the data with exception for the region between 3.5 to 5 GeV where offsets of order 1σ are indicated. The NuWro prediction falls below the data in the two lowest $E_{\bar{\nu}}$ bins, but matches the data to within 1σ throughout the higher $E_{\bar{\nu}}$ range. The GIBUU-2017 prediction, however, lies below the data at all energies. The lower plot shows the relative cross-section portions that arise from the four interaction

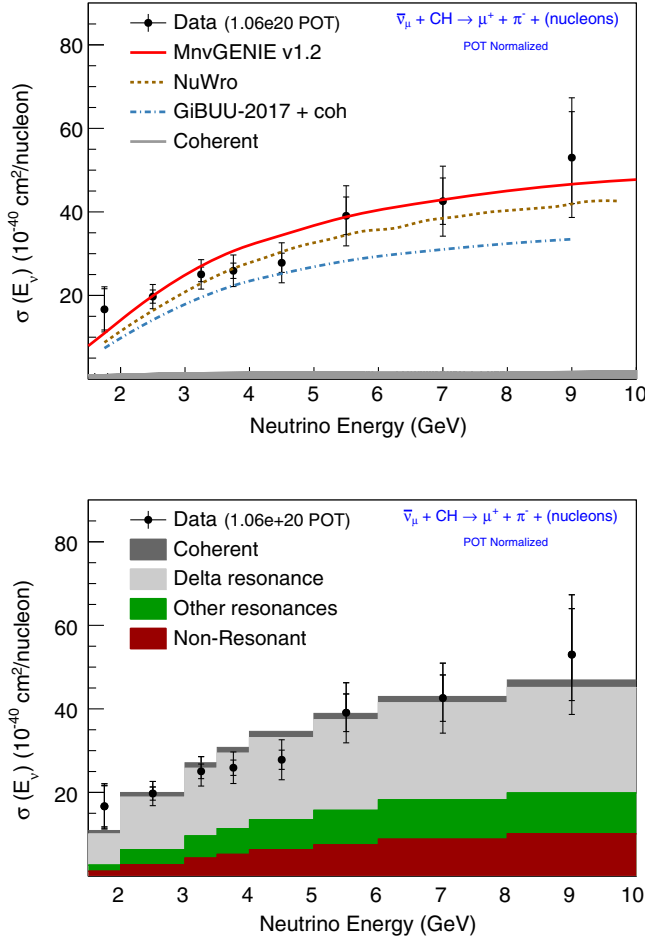


FIG. 14. Cross section (solid circles) as a function of antineutrino energy for channel (1). Upper plot compares the data to GENIE, NuWro, and GiBUU-2017 expectations. Lower plot shows contributions estimated by GENIE from coherent scattering, Δ^- resonance production, N^* states above the Δ , and pion nonresonance processes.

categories utilized by GENIE. The relative contributions are predicted to remain in roughly constant proportion throughout the measured $E_{\bar{\nu}}$ range, with Δ production being dominant throughout.

The squared four-momentum transfer from the lepton system, Q^2 , is calculated using Eq. (5); the differential cross section, $d\sigma/dQ^2$, is shown in Fig. 15. Comparisons with GENIE, NuWro, and GiBUU-2017 predictions are presented in the upper plot, and the relative contributions from the major reaction categories as estimated by GENIE are given in the lower plot. A contribution from CC coherent scattering reaction (4) is estimated to occur in the region $Q^2 < 0.4 \text{ GeV}^2$. The amount shown by the gray (dark gray) histograms in the upper (lower) plot is the rate expected from MINERvA measurements [8]. The data points in Fig. 15 include this CC coherent scattering contribution.

Even with allowance made for the presence of CC coherent scattering, the data do not exhibit a turnover in

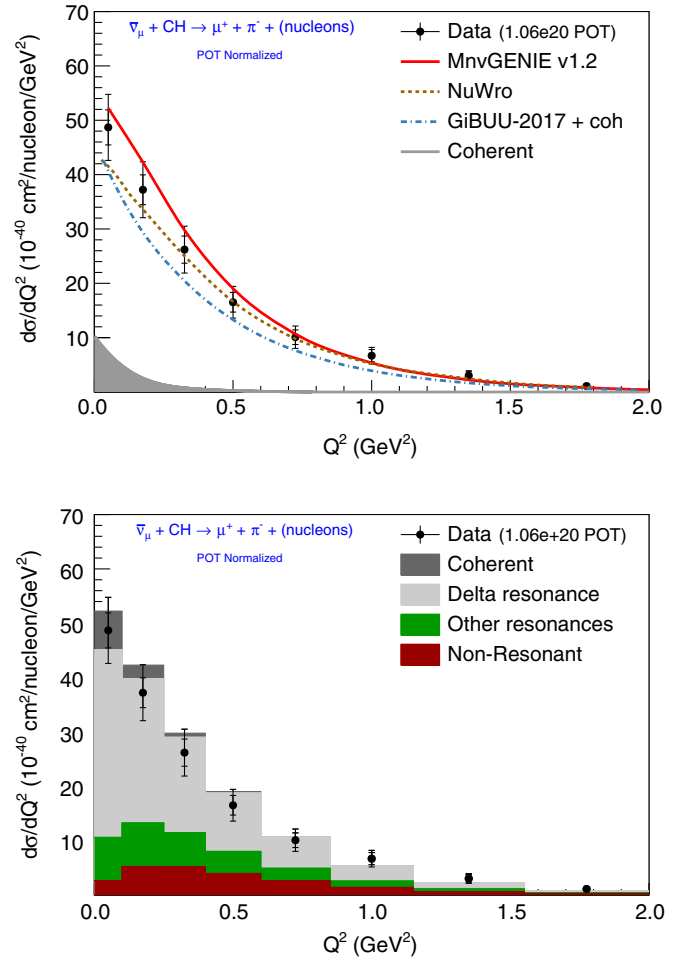


FIG. 15. Differential cross section $d\sigma/dQ^2$ for the signal channel. Upper plot: Predictions from the GENIE-based MC, NuWro, and GiBUU-2017 trend above, close to, and below the data respectively. Lower plot: Relative contributions from component processes according to GENIE. Coherent single-pion production is expected to contribute at very low Q^2 .

$d\sigma/dQ^2$ as Q^2 approaches zero. The absence of a turnover distinguishes the signal channel (1) of this work from the antineutrino and neutrino CC(π^0) channels previously studied by MINERvA [11,13]. This may be evidence for a process similar to CC coherent scattering that populates the low Q^2 region of reactions (2) and (3), but does not participate in reactions in which the target nucleon changes its identity, such as $\bar{\nu}_\mu p \rightarrow \mu^+ \pi^0 n$. Charged-current diffractive scattering on nucleons is such a process, and its presence in high energy neutrino scattering has been pointed out by D. Rein [79]. According to Rein, CC diffractive pion production must also be present in lower- E_ν scattering but its effect becomes very hard to disentangle from other CC(π) processes.

In measurements of neutrino-induced CC(π) channels carried out by MiniBooNE [74,80] and by MINOS [81], it was found that MC agreement with data can be improved

by introducing, *ad hoc*, a suppression of baryon-resonance production at low Q^2 . This approach finds some support from Q^2 -dependent reductions that ensue with theoretical treatments of nuclear medium effects that go beyond the Fermi gas model [82–86]. Figure 15 suggests that low- Q^2 suppression may not be a universal feature of charged-current pion production channels in $\nu_\mu/\bar{\nu}_\mu$ nucleus scattering.

XII. ESTIMATION OF $\bar{\nu}_\mu$ -NUCLEON CROSS SECTIONS IN HYDROCARBON

The definition of signal channel (1) that the analysis has used up to this point refers to final-state topologies as they emerge from target nuclei. This signal definition is constructed such that all selections refer to directly observable quantities, and the differential cross sections subsequently presented refer to final-states that have been subjected to hadronic FSI. Cross sections in this form provide direct tests and feedback for continued development of neutrino event generators, as has been elaborated in Secs. IX–XI.

It is nevertheless of interest to investigate whether cross sections measured in a hydrocarbon medium can be related to the underlying initial antineutrino-nucleon interactions. The CC(π) cross sections reported by the bubble chamber experiments of the 1970s and 1980s, including those using propane-freon as well as deuterium or hydrogen fills, are entirely of the (anti)-neutrino plus quasifree nucleon kind [14–20]. Such measurements require fine-grained event imaging and rely upon certain aspects of neutrino-interaction modeling, e.g., Fermi motion and hadronic FSI. Their pursuit has not been taken up by spectrometer experiments of the modern era. With the present analysis however, there arises motivation to undertake determinations of the exclusive-channel cross sections for reactions (2) and (3). Two factors contribute to the feasibility of making these measurements with MINERvA:

- (i) First, it is possible to relate the event rate determined for the signal channel into component rates for which the main contributors are the “initial” (prior to FSI) quasifree nucleon reactions (2) and (3). In this approach the focus is placed on the initial $\bar{\nu}_\mu$ -nucleon interactions that occur in target nuclei prior to any final-state alterations that may occur with the final-state hadrons as they traverse the parent nucleus. These two initial reactions are now to be regarded as “the signal,” while other initial reactions which, upon emergence from the parent nucleus, have morphed into channel (1), are now regarded to be “background.” The two aforementioned as-born signal reactions differ according to the interaction nucleon that accompanies the muon and pion; the final-state hadronic systems are (n π^-) and (p π^-) respectively. Their different charge content gives a measurable differences between distributions of vertex energy for the two final states. While the

distribution shapes must be taken from the reference simulation, the relative rates are well-constrained by fitting to the vertex energy distribution observed in the signal sample, as is described in Sec. XII A below.

- (ii) Second, the GENIE-based reference MC appears to describe hadronic FSI in carbon rather well, and the MC generally succeeds with shape predictions for backgrounds. Importantly, there is no indication in previous $\bar{\nu}_\mu$ and ν_μ CC(π) measurements of large spectral distortions arising from 2p2h production [10,11,13].

These two factors are important because the analysis—in order to ascertain the relative rates of the two initial, pre-FSI final states—must rely on the hadronic FSI model of the reference simulation.

This approach is pursued in paragraphs below and cross sections are obtained for the exclusive reactions (2) and (3). Comparisons are made with measurements obtained with large bubble chambers.

With exclusive-reaction cross sections for (2) and (3) in hand, it becomes possible to relate them to the MINERvA measurement of $\bar{\nu}_\mu$ -CC(π^0) reported in Refs. [10,11]. Of course, such a comparison requires the latter measurement to be subjected to the same approach—one that elicits the underlying initial reaction rate. The opportunity then arises to decompose the three (noncoherent) exclusive reactions of $\bar{\nu}_\mu$ -CC(π) production in terms of the underlying isospin $I = 3/2$ and $I = 1/2$ amplitudes. A MINERvA-based isospin decomposition of $\bar{\nu}_\mu$ -CC(π) is reported in Sec. XIII.

A. Channel separation using vertex energy

The selected signal sample prior to background subtraction can be regarded as originating from four processes. In addition to events of reactions (2) and (3), there are contributions from CC coherent scattering reaction (4) and from background reactions. The relative contributions of these processes to the signal channel rate can be distinguished by examining the “vertex energy” distribution of the signal sample. For the purpose of this analysis, vertex energy is defined to be the sum of energies of ionization hits deposited within 10 cm of the primary vertex that is unassociated with the μ^+ and π^- tracks. That vertex energy is a measurable quantity is illustrated by the event displays in Fig. 1.

Figure 16 shows the distribution of vertex energy in signal-sample candidates (solid circles, statistical errors). In the upper plot, which displays the distribution using a linear scale, it is readily seen that nearly two-thirds of the sample has ≤ 5 MeV of vertex energy and falls within the first bin. Events of the rest of the sample have vertex energies that lie in the higher range extending from 5 MeV to 100 MeV. In order to provide a clearer picture of this higher energy range, the same event distribution is displayed in the lower plot of Fig. 16 using a logarithmic scale.

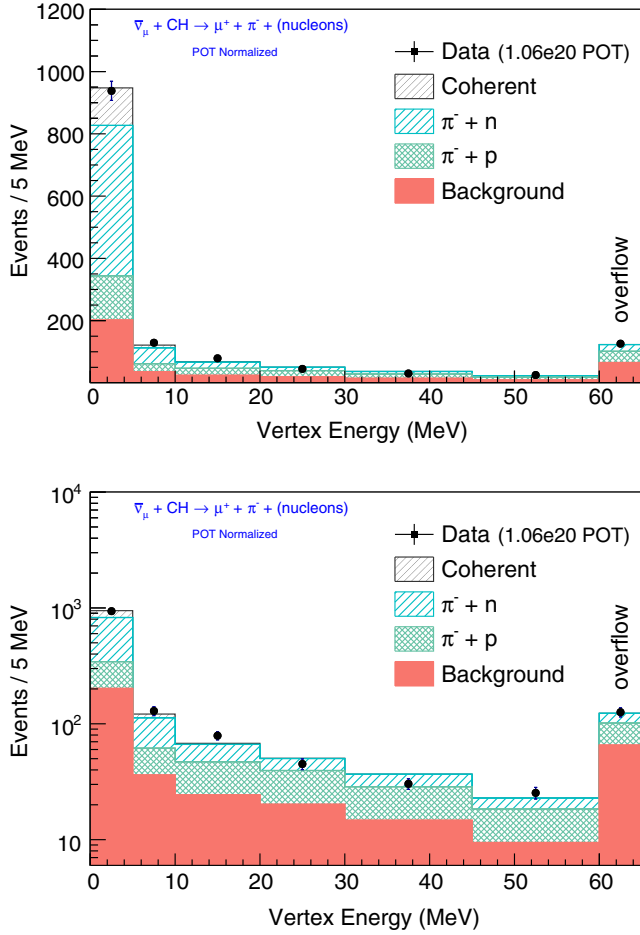


FIG. 16. Distribution of event vertex energy in the signal sample (solid circles), displayed using linear and log scales (upper, lower plots respectively). Reference MC predictions for contributions by reactions (2) and (3), labeled by their hadronic systems, are shown together with coherent scattering and background contributions. The coherent contribution is calculated from MINERvA measurement [8]; the background rate is constrained by sideband fitting, and the exclusive-reaction rates are tuned to fit the signal sample data.

The MC component histograms in Fig. 16 show the estimated contributions from the four processes. The breakout shown is obtained after three procedures have been applied:

- (i) The coherent scattering contribution (top histogram, shaded) is fixed according to the measurement of reaction (4) by MINERvA [8].
- (ii) The contribution from background is determined using a sideband constraint in the manner described for the main analysis, but with care taken concerning the signal definition which for the present purpose has been changed. Referring to the reference MC model for the sideband distribution of vertex energy, the “signal” are events that originated from reactions

(2), (3), and (4), while everything else is background. The distribution shapes for signal and background are taken from the reference MC, and their absolute normalizations are determined by iterative fitting between data of the sideband (to set the background normalization) and data of the analysis signal sample (to refine the estimate of signal contamination in the sideband).

- (iii) With the background and coherent scattering contributions thereby set, a fit to the vertex energy data is performed wherein the distribution shapes for reaction (2) and (3) contributions are taken from the reference simulation, and their normalizations are used as fit parameters.

It is readily seen in Fig. 16 that the fit adjustment of the MC model gives a good description of the data. Based on this description, the numbers of interactions (2) and (3) that underwrite the signal-sample population are estimated to be $N(\mu^+ n \pi^-) = 682 \pm 121$ and $N(\mu^+ p \pi^-) = 349 \pm 121$, where the error bars include systematic as well as statistical uncertainties. To convert these event counts into cross sections, it is required to know the efficiencies with which the analysis selection chain retains the progeny of reactions (2) and (3) and allows them to appear in the selected signal sample. These efficiencies, as estimated by the reference simulation, are $\epsilon(\mu^+ \pi^- n) = 4.9\%$ and $\epsilon(\mu^+ \pi^- p) = 4.1\%$. The hydrocarbon target region of MINERvA contains 15% more protons than neutrons. The difference is taken into account in order to obtain exclusive-channel cross sections that are “per nucleon” for an isoscalar target medium. The cross section values are

$$\sigma(\mu^+ \pi^- n) = 19.7 \pm 4.4 \times 10^{-40} \text{ cm}^2 \text{ per nucleon}, \quad (8)$$

$$\sigma(\mu^+ \pi^- p) = 12.1 \pm 4.5 \times 10^{-40} \text{ cm}^2 \text{ per nucleon}. \quad (9)$$

Comparable results are the flux-averaged cross sections for $W < 2$ GeV based on Gargamelle antineutrino data. These are stated without errors in Table VII of Ref. [29] as follows: $\sigma(\mu^+ \pi^- n) = 25.1 \times 10^{-40} \text{ cm}^2$ and $\sigma(\mu^+ \pi^- p) = 10.1 \times 10^{-40} \text{ cm}^2$. Table 3 and Figs. 2 and 3 of Ref. [14], indicate uncertainties for these cross sections (arising from background correction, nuclear effects, and finite statistics) to be of order 25%.

XIII. ISOSPIN COMPOSITION OF $\bar{\nu}_\mu$ -CC(π)

A broader perspective on $\bar{\nu}_\mu$ -CC(π) reactions can be obtained by relating the MINERvA measurement of $\bar{\nu}_\mu$ -CC(π^0) [10,11] to cross sections (8) and (9). To this end, a reanalysis of the latter data has been carried out to extract the free-proton target cross section for the exclusive channel

$$\bar{\nu}_\mu + p \rightarrow \mu^+ + \pi^0 + n. \quad (10)$$

The measured signal channel of $\bar{\nu}_\mu$ -CC(π^0) is devoid of any coherent scattering contribution, and exclusive reaction (10) is the only $\bar{\nu}_\mu$ -nucleon interaction that feeds the signal channel. Consequently the extraction of the reaction (10) cross section is relatively straightforward. The event selections described in Secs. III–V are applied in the same way to the data of the earlier work. As previously noted, a weight is applied to normalize the cross section for reaction (10) to describe scattering per nucleon from an isoscalar target. The “as born” free-nucleon target cross section for reaction (10) thereby obtained is

$$\sigma(\mu^+ \pi^0 n) = 10.7 \pm 1.7 \times 10^{-40} \text{ cm}^2 \text{ per nucleon.} \quad (11)$$

The flux-averaged value for $W < 2$ GeV attributed to Gargamelle [29] is $\sigma(\mu^+ \pi^0 n) = 9.5 \times 10^{-40} \text{ cm}^2$.

The cross sections (8), (9), and (11) as hereby extracted from MINERvA data, comprise the complete set of free-nucleon cross sections for exclusive $\bar{\nu}_\mu$ -CC(π) reactions. Each of these reactions proceeds via the $\Delta S = 0$ weak hadronic charged current; The current operator transforms as an isovector. This has the consequence that the final states of (2), (3), and (10) can be expressed in terms of reduced amplitudes A_3 and A_1 which describe the $I = 3/2$ and $I = 1/2$ states of the πN system. These amplitudes (in the convention of Rein-Sehgal [29]) can be written as

$$\begin{aligned} A(\bar{\nu} n \rightarrow \mu^+ n \pi^-) &= \sqrt{2} A_3, \\ A(\bar{\nu} p \rightarrow \mu^+ n \pi^0) &= \frac{2}{3} (A_3 - A_1), \\ A(\bar{\nu} p \rightarrow \mu^+ p \pi^-) &= \frac{\sqrt{2}}{3} (A_3 + 2A_1). \end{aligned}$$

Relations are thereby implied that interrelate these cross sections. For example, if the $\Delta(1232)$ dominates a selected kinematic region such that $|A_3| \gg |A_1|$, then one expects certain cross section ratios to exhibit particular values. Specifically, for the ratios

$$\begin{aligned} R_1 &\equiv \sigma(\mu^+ n \pi^0) / \sigma(\mu^+ n \pi^-), \quad \text{and} \\ R_2 &\equiv \sigma(\mu^+ p \pi^-) / \sigma(\mu^+ n \pi^-), \end{aligned}$$

one expects $R_1 \simeq 2/9$ and $R_2 \simeq 1/9$ for the case of A_3 dominance. As shown below, the data does not support this particular scenario.

More generally, the flux-averaged free-nucleon cross sections for (2), (3), and (10) in the hadronic mass range $W < 1.8$ GeV, enable values to be obtained for the following averaged quantities [29]:

$$\begin{aligned} \langle |A_3|^2 \rangle &= \frac{1}{2} \sigma(\mu^+ n \pi^-), \\ \langle |A_1|^2 \rangle &= \frac{3}{4} \left\{ \sigma(\mu^+ n \pi^0) + \sigma(\mu^+ p \pi^-) - \frac{1}{3} \sigma(\mu^+ n \pi^-) \right\}, \\ \langle \mathcal{R}e(A_3^* A_1) \rangle &= \frac{3}{8} \left\{ \sigma(\mu^+ p \pi^-) - 2\sigma(\mu^+ n \pi^0) + \frac{1}{3} \sigma(\mu^+ n \pi^-) \right\}. \end{aligned}$$

The relative magnitude of the two isospin amplitudes, $R^{\bar{\nu}}$, and their relative phase, $\phi^{\bar{\nu}}$, are given by the relations

$$\begin{aligned} R^{\bar{\nu}} &= \{ \langle |A_1|^2 \rangle / \langle |A_3|^2 \rangle \}^{1/2}, \\ \cos \phi^{\bar{\nu}} &= \langle \mathcal{R}e(A_3^* A_1) \rangle / \langle |A_3|^2 \rangle^{1/2} \langle |A_1|^2 \rangle^{1/2}. \end{aligned}$$

The above quantities can be written as functions of the CC(π) cross sections or as functions of R_1 and R_2 . (See Eqs. (4.8) and (4.9) of Ref. [29].)

A. MINERvA results

Using the cross-section values (8), (9), and (11) this analysis obtains $R_1 = 0.46 \pm 0.08$ and $R_2 = 0.52 \pm 0.19$. The relative magnitude and phase of the isospin amplitudes are then determined to be

$$R^{\bar{\nu}} = 0.99 \pm 0.19, \quad \phi^{\bar{\nu}} = 93^\circ \pm 7^\circ. \quad (12)$$

The $R^{\bar{\nu}}$ value indicates a large presence for the $I = 1/2$ amplitude in the final states of $\bar{\nu}_\mu$ -CC(π). The value for $\phi^{\bar{\nu}}$ indicates that A_3 and A_1 are, on average, roughly 90° out of phase. These observations are consistent with a resonant $I = 3/2$ amplitude whose phase is rotating counterclockwise through $\pi/2$ (at the Δ peak), while the phase of the nonresonant $I = 1/2$ amplitude remains stationary near 0° .

B. Bubble chamber measurements

The isospin decomposition reported here was originally utilized by bubble chamber experiments of the 1970s and 1980s. A full determination of $R^{\bar{\nu}}$ and $\phi^{\bar{\nu}}$ for the $\bar{\nu}_\mu$ -CC(π) channels was carried out using the Gargamelle bubble chamber filled with a light propane-freon mixture [14]. Table I compares the present MINERvA measurement with the Gargamelle result. The measurement precisions are seen to be roughly comparable, reflecting the fact that MINERvA’s statistical advantage (factor ~ 2.2 in event candidates) is partially offset by systematic uncertainties that are larger than those incurred with the bubble chamber technique. Together, the two experiments give a very consistent picture of the isospin composition of $\bar{\nu}_\mu$ -CC(π) channels.

Under the assumption that the $\Delta S = 0$ charged current operator is charge symmetric, antineutrino reactions $\bar{\nu} + (-I_3^i) \rightarrow \mu^+ + (-I_3^f)$ may be related to neutrino reactions $\nu + (I_3^i) \rightarrow \mu^- + (I_3^f)$, where the initial and final hadronic systems are labeled by their I_3 values. This relation

TABLE I. Antineutrino measurements of relative strength, $R^{\bar{\nu}}$, and relative phase, $\phi^{\bar{\nu}}$, for isospin 1/2 and 3/2 amplitudes of $\bar{\nu}_\mu$ -CC(π) production. Results of this work (lower rows, leftmost columns) are in good agreement with values obtained four decades ago using the Gargamelle bubble chamber.

Experiment medium	$\bar{\nu}$ flux [GeV]	W [GeV]	$R^{\bar{\nu}}$	$\phi^{\bar{\nu}}$ degrees
Gargamelle [14]	~ 0.5 – 10.0	≤ 1.8	1.14 ± 0.23	$94 \pm 13^\circ$
Propane-freon	peak: 1.5	≤ 1.4	0.98 ± 0.20	$\{90^\circ\}$
MINERvA	~ 1.5 – 10.0	≤ 1.8	0.99 ± 0.19	$93 \pm 7^\circ$
Hydrocarbon	peak: 3.0			

motivates a comparison of the isospin amplitude relations of the present work to those obtained by the large bubble chamber experiments in analysis of neutrino-induced single pion production. Decomposition of the three exclusive channels of ν_μ -CC(π) proceeds as previously described, but with cross sections (8), (9), and (11) replaced by $\sigma(\mu^- \pi^+ p)$, $\sigma(\mu^- \pi^+ n)$, and $\sigma(\mu^- \pi^0 p)$ respectively. The bubble-chamber measurements for R^ν and ϕ^ν of neutrino-induced πN systems are summarized in Table II. As with the $\bar{\nu}_\mu$ -CC(π) results, the ν_μ measurements also find the $I = 1/2$ amplitude to be sizable relative to the resonant $I = 3/2$ amplitude, and indicate the two amplitudes to be 90° out of phase on average.

A discernible trend in the neutrino results is that higher reach in W correlates with larger R^ν values. This is understandable because, above $W > 1.4$ GeV, the $\Delta(1232)$ contribution is diminished while $I = 1/2$ baryon resonances gain strength. The MINERvA data contain a relatively large contribution from events with W between 1.4–1.8 GeV compared to the ANL and BNL data sets, and this may be the reason why $R^{\bar{\nu}}$ of MINERvA is larger than R^ν as measured by ANL and BNL.

A convenient way to compare measurements of the relative magnitude and phase of A_1 vs A_3 is with the diplot shown in Fig. 17. The plot maps measurements of the cross-section ratios R_1 and R_2 onto a coordinate grid of slanted dashed lines and solid-line curves that denote values of $R^{\bar{\nu}}$ and $\phi^{\bar{\nu}}$ respectively. The MINERvA and

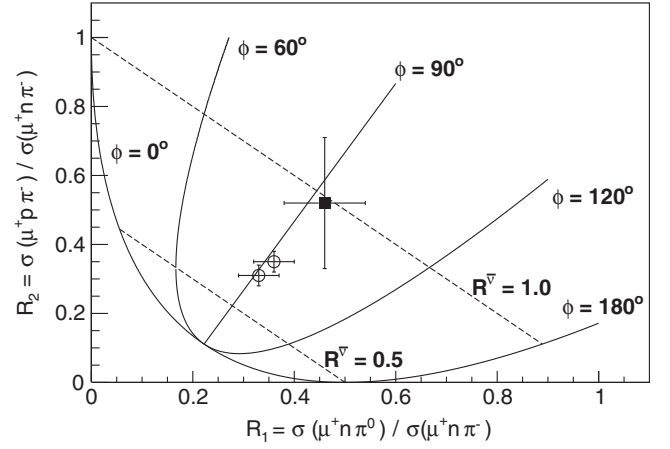


FIG. 17. Plot of the cross section ratios R_2 vs R_1 for selected $\bar{\nu}_\mu$ and ν_μ data. Dashed lines denote constant values of $|A_1|/|A_3|$ and solid-line curves denote values of the relative phase. The MINERvA measurements (solid square), as with Gargamelle (not plotted; see Table I) show that A_1 and A_3 , averaged over a wide-band $\bar{\nu}$ flux, are of similar strength and devoid of interference. Results obtained with ν_μ -CC(π) reactions from overlapping samples indicate $|A_3| > |A_1|$ in neutrino samples at lower incident energies and lesser reach in W [88].

Gargamelle antineutrino measurements lie within 1σ of $(R^{\bar{\nu}}, \phi^{\bar{\nu}}) \simeq (1.0, 90^\circ)$, indicating the amplitude strengths to be nearly equal and non-interfering ($\cos \phi^{\bar{\nu}} \simeq 0$). The neutrino measurements, working with lower- W samples, also lie along the $\phi = 90^\circ$ axis but at R^ν values distinctly less than 1.0. The plot suggests that the representation point for a CC(π) sample migrates upward along $\phi^\nu = 90^\circ$, as the average W of the sample is increased.

XIV. CONCLUSIONS

A study of semiexclusive $\bar{\nu}_\mu$ -CC(π^-) scattering on hydrocarbon is reported using $\bar{\nu}_\mu$ interactions with $E_{\bar{\nu}}$ ranging from ~ 1.5 to 10 GeV, with final-state $W < 1.8$ GeV. This is the first experiment working in the few-GeV region of incident $\bar{\nu}_\mu$ to report differential cross sections for μ^+ and π^- kinematic variables θ_μ , p_μ , T_π , and θ_π , while also reporting

TABLE II. Neutrino bubble chamber measurements of relative strength and phase for the isospin 1/2 and 3/2 amplitudes of neutrino-induced CC(π) production. Values obtained for neutrino-induced R^ν and ϕ^ν are similar to those reported in Table I for antineutrino single-pion production.

Experiment medium	ν flux [GeV]	W [GeV]	R^ν	ϕ^ν degrees
Gargamelle [15]	~ 0.5 – 10.0	≤ 1.4	0.71 ± 0.14	$75^{+12^\circ}_{-16^\circ}$
Propane-freon	peak: 1.5	All data	1.03 ± 0.15	$73^{+12^\circ}_{-10^\circ}$
BNL 7' BC [87]	< 3.0	≤ 1.4	0.60 ± 0.07	$90 \pm 11^\circ$
Deuterium	peak: 1.0	≤ 1.6	0.79 ± 0.05	$95 \pm 7^\circ$
		All data	0.89 ± 0.05	$97 \pm 6^\circ$
ANL 12' BC [88]	< 1.5	≤ 1.4	0.68 ± 0.04	$90.7 \pm 4.6^\circ$
Deuterium	peak: 0.5	≤ 1.6	0.75 ± 0.04	$92.0 \pm 4.1^\circ$

cross sections as functions of $E_{\bar{\nu}}$ and Q^2 . Data summary tables for these measurements that may facilitate phenomenological investigations are available in the Supplemental Material [76].

Measured differential cross sections are compared to predictions based upon the GENIE, NuWro, and GiBUU-2017 event generators. The predictions generally reproduce the shapes of the differential cross sections, with $d\sigma/d\theta_{\pi^-}$ being the sole exception. The event generators differ with respect to predictions for absolute event rate. The GENIE-based simulation gives the highest event rate and its prediction exceeds the observed data rate by 8%.

The shape of the pion T_π differential cross section is considered in light of GENIE's effective cascade treatment of processes that comprise pion FSI. The modeling provides a detailed picture for the $d\sigma/T_\pi$ distribution that is consistent with the data (Fig. 12). This same picture suggests that adjustments to pion FSI elastic and inelastic scattering that promote emission into smaller, more forward angles may be in order (Fig. 13). For $d\sigma/dQ^2$, neither the data nor the generator curves exhibit a turn-over in the distribution at very-low Q^2 . This observation contrasts with distribution turn-over for $Q^2 < 0.20 \text{ GeV}^2$ that occurs in MINERvA measurements for $\bar{\nu}_\mu\text{-CC}(\pi^0)$ [10] and $\nu_\mu\text{-CC}(\pi^0)$ channels [11,13].

The signal sample has been decomposed into $\bar{\nu}_\mu$ interactions of four kinds, with exclusive reactions (2) and (3) being the major contributors. Flux-averaged quasifree nucleon scattering cross sections are presented in Eqs. (8) and (9). The flux-averaged cross section (11) is extracted from the published MINERvA measurement of $\bar{\nu}_\mu\text{-CC}(\pi^0)$. These three $\bar{\nu}_\mu$ -nucleon cross sections are used to carry out an isospin decomposition of CC single pion production initiated by antineutrino (noncoherent) interactions. The relative magnitude and phase of isospin amplitudes A_1 and A_3 presented in Eq. (12) are in agreement with the pioneering Gargamelle measurement [14].

In summary, the measurements of this work introduce a wealth of new information about $\bar{\nu}_\mu\text{-CC}(\pi)$, an antineutrino interaction channel that features prominently in data samples being recorded by the long-baseline experiments.

These results pave the way for more precise determinations of the fundamental parameters that govern flavor oscillations of neutrinos and antineutrinos.

ACKNOWLEDGMENTS

This document was prepared by members of the MINERvA Collaboration using the resources of the Fermi National Accelerator Laboratory (Fermilab), a U.S. Department of Energy, Office of Science, HEP User Facility. Fermilab is managed by Fermi Research Alliance, LLC (FRA), acting under Contract No. DE-AC02-07CH11359. These resources included support for the MINERvA construction project, and support for construction also was granted by the United States National Science Foundation under Grant No. PHY-0619727 and by the University of Rochester. Support for participating scientists was provided by NSF and DOE (USA); by CAPES and CNPq (Brazil); by CoNaCyT (Mexico); by Proyecto Basal FB 0821, CONICYT PIA ACT1413, Fondecyt 3170845 and 11130133 (Chile); by CONCYTEC (Consejo Nacional de Ciencia, Tecnología e Innovación Tecnológica), DGI-PUCP (Dirección de Gestión de la Investigación—Pontificia Universidad Católica del Perú), and VRI-UNI (Vice-Rectorate for Research of National University of Engineering) (Peru); and by the Latin American Center for Physics (CLAF); NCN Opus Grant No. 2016/21/B/ST2/01092 (Poland); by Science and Technology Facilities Council (UK). We thank the MINOS Collaboration for use of its near detector data. Finally, we thank the staff of Fermilab for support of the beam line, the detector, and computing infrastructure. This manuscript has been authored by Fermi Research Alliance, LLC under Contract No. DE-AC02-07CH11359 with the U.S. Department of Energy, Office of Science, Office of High Energy Physics. The United States Government retains and the publisher, by accepting the article for publication, acknowledges that the United States Government retains a non-exclusive, paid-up, irrevocable, world-wide license to publish or reproduce the published form of this manuscript, or allow others to do so, for United States Government purposes.

[1] K. Abe *et al.* (T2K Collaboration), *Nucl. Instrum. Methods Phys. Res., Sect. A* **659**, 106 (2011).
 [2] D. S. Ayres *et al.* (NOvA Collaboration), CERN Report No. FERMILAB-DESIGN-2007-01, 2007.
 [3] <http://www.dunescience.org/>.
 [4] K. Abe *et al.* (T2K Collaboration), *Phys. Rev. Lett.* **121**, 171802 (2018).

[5] M. A. Acero *et al.* (NOvA Collaboration), *Phys. Rev. D* **98**, 032012 (2018).
 [6] T. Katori and M. Martini, *J. Phys. G* **45**, 013001 (2018).
 [7] A. Higuera *et al.* (MINERvA Collaboration), *Phys. Rev. Lett.* **113**, 261802 (2014).
 [8] A. Mislivec, A. Higuera *et al.* (MINERvA Collaboration), *Phys. Rev. D* **97**, 032014 (2018).

- [9] K. Abe *et al.* (Hyper-Kamiokande Proto-Collaboration), *Prog. Theor. Exp. Phys.* **2015**, 053C02 (2015).
- [10] T. Le *et al.* (MINERvA Collaboration), *Phys. Lett. B* **749**, 130 (2015).
- [11] C. L. McGivern, T. Le, B. Eberly *et al.* (MINERvA Collaboration), *Phys. Rev. D* **94**, 052005 (2016).
- [12] B. Eberly *et al.* (MINERvA Collaboration), *Phys. Rev. D* **92**, 092008 (2015).
- [13] O. Altinok, T. Le *et al.* (MINERvA Collaboration), *Phys. Rev. D* **96**, 072003 (2017).
- [14] T. Bolognese, J. P. Engel, J. L. Guyonnet, and J. L. Riestler (Gargamelle Collaboration), *Phys. Lett.* **81B**, 393 (1979).
- [15] M. Pohl *et al.* (Gargamelle Collaboration), *Lett. Nuovo Cimento* **24**, 540 (1979).
- [16] H. J. Grabosch *et al.* (SKAT Collaboration), *Z. Phys. C* **41**, 527 (1989).
- [17] S. J. Barish *et al.*, *Phys. Lett.* **91B**, 161 (1980).
- [18] D. Allasia *et al.* (Asterdam-Bologna-Padova-Pisa-Saclay-Torino Collaboration), *Z. Phys. C* **20**, 95 (1983).
- [19] D. Allasia *et al.* (Amsterdam-Berge-Bologna-Padov-Pisa-Saclay-Torino Collaboration), *Nucl. Phys.* **B343**, 285 (1990).
- [20] P. Allen *et al.* (Aachen-Birmingham-Bonn-CERN-London IC-Munich-Oxford Collaboration), *Nucl. Phys.* **B264**, 221 (1986).
- [21] P. Adamson *et al.*, *Nucl. Instrum. Methods Phys. Res., Sect. A* **806**, 279 (2016).
- [22] E. A. Paschos and D. Schalla, arXiv:1209.4219.
- [23] E. B. Martinez, A. Mariano, and C. Barbero, *J. Phys. Soc. Jpn. Conf. Proc.* **12**, 010042 (2016).
- [24] U. Mosel, *Phys. Rev. C* **91**, 065501 (2015).
- [25] R. González-Jiménez, N. Jachowicz, K. Niewczas, J. Nys, V. Pandey, T. Van Cuyck, and N. Van Dessel, *Phys. Rev. D* **95**, 113007 (2017).
- [26] R. González-Jiménez, K. Niewczas, and N. Jachowicz, *Phys. Rev. D* **97**, 013004 (2018).
- [27] J. E. Sobczyk, E. Hernandez, S. X. Nakamura, J. Nieves, and T. Sato, *Phys. Rev. D* **98**, 073001 (2018).
- [28] M. Kabirmezahad, *Phys. Rev. D* **97**, 013002 (2018).
- [29] D. Rein and L. M. Sehgal, *Ann. Phys. (N.Y.)* **133**, 79 (1981).
- [30] D. Rein, *Z. Phys. C* **35**, 43 (1987).
- [31] L. Aliaga *et al.* (MINERvA Collaboration), *Nucl. Instrum. Methods Phys. Res., Sect. A* **743**, 130 (2014).
- [32] L. Aliaga *et al.* (MINERvA Collaboration), *Nucl. Instrum. Methods Phys. Res., Sect. A* **789**, 28 (2015).
- [33] D. G. Michael *et al.* (MINOS Collaboration), *Nucl. Instrum. Methods Phys. Res., Sect. A* **596**, 190 (2008).
- [34] C. M. Marshall *et al.* (MINERvA Collaboration), *Phys. Rev. D* **94**, 012002 (2016).
- [35] S. Agostinelli, J. Allison, K. Amako, J. Apostolakis, H. Araujo *et al.*, *Nucl. Instrum. Methods Phys. Res., Sect. A* **506**, 250 (2003).
- [36] J. Allison *et al.*, *IEEE Trans. Nucl. Sci.* **53**, 270 (2006).
- [37] C. Alt *et al.* (NA49 Collaboration), *Eur. Phys. J. C* **49**, 897 (2007).
- [38] D. S. Barton *et al.*, *Phys. Rev. D* **27**, 2580 (1983).
- [39] A. V. Lebedev, Ph. D Thesis, Harvard University Report No. FERMILAB-THESIS-2007-76, 2007.
- [40] L. Aliaga *et al.* (MINERvA Collaboration), *Phys. Rev. D* **94**, 092005 (2016).
- [41] J. Park *et al.* (MINERvA Collaboration), *Phys. Rev. D* **93**, 112007 (2016).
- [42] C. E. Patrick *et al.* (MINERvA Collaboration), *Phys. Rev. D* **97**, 052002 (2018).
- [43] C. Andreopoulos *et al.* (GENIE Collaboration), *Nucl. Instrum. Methods Phys. Res., Sect. A* **614**, 87 (2010).
- [44] P. A. Rodrigues *et al.* (MINERvA Collaboration), *Phys. Rev. Lett.* **116**, 071802 (2016).
- [45] L. Ren *et al.* (MINERvA Collaboration), *Phys. Rev. D* **95**, 072009 (2017).
- [46] M. Betancourt, A. Ghosh, T. Walton *et al.* (MINERvA Collaboration), *Phys. Rev. Lett.* **119**, 082001 (2017).
- [47] R. Gran *et al.* (MINERvA Collaboration), *Phys. Rev. Lett.* **120**, 221805 (2018).
- [48] X.-G. Lu *et al.* (MINERvA Collaboration), *Phys. Rev. Lett.* **121**, 022504 (2018).
- [49] D. Ruterbories *et al.* (MINERvA Collaboration), *Phys. Rev. D* **99**, 012004 (2019).
- [50] A. Bodek and J. L. Ritchie, *Phys. Rev. D* **23**, 1070 (1981).
- [51] J. Beringer *et al.* (Particle Data Group), *Phys. Rev. D* **86**, 010001 (2012).
- [52] A. Bodek, I. Park, and U. Yang, *Nucl. Phys. B, Proc. Suppl.* **139**, 113 (2005).
- [53] H. Gallagher, *Nucl. Phys. B, Proc. Suppl.* **159**, 229 (2006).
- [54] C. Wilkinson, P. Rodrigues, S. Cartwright, L. Thompson, and K. McFarland, *Phys. Rev. D* **90**, 112017 (2014).
- [55] P. Rodrigues, C. Wilkinson, and K. McFarland, *Eur. Phys. J. C* **76**, 474 (2016).
- [56] S. A. Dytman and A. S. Meyer, *AIP Conf. Proc.* **1405**, 213 (2011).
- [57] J. Nieves, I. Ruiz Simo, and M. J. Vicente Vacas, *Phys. Lett. B* **707**, 72 (2012).
- [58] R. Gran, J. Nieves, F. Sanchez, and M. J. Vicente Vacas, *Phys. Rev. D* **88**, 113007 (2013).
- [59] J. Nieves, J. E. Amaro, and M. Valverde, *Phys. Rev. C* **70**, 055503 (2004); **72**, 019902(E) (2005).
- [60] D. Rein and L. M. Sehgal, *Phys. Lett. B* **657**, 207 (2007).
- [61] T. Golan, C. Juszczak, and J. T. Sobczyk, *Phys. Rev. C* **86**, 015505 (2012).
- [62] O. Buss, T. Gaitanos, K. Gallmeister, H. van Hees, M. Kaskulov, O. Lalakulich, A. B. Larionov, T. Leitner, J. Weil, and U. Mosel (GIBUU Collaboration), *Phys. Rep.* **512**, 1 (2012).
- [63] GiBUU Collaboration, <http://gibuu.hepforge.org> (2014).
- [64] S. L. Adler, *Ann. Phys. (N.Y.)* **50**, 189 (1968).
- [65] S. L. Adler, *Phys. Rev. D* **12**, 2644 (1975).
- [66] L. L. Salcedo, E. Oset, M. J. Vicente-Vacas, and C. Garcia-Recio, *Nucl. Phys.* **A484**, 557 (1988).
- [67] J. T. Sobczyk and J. Zmuda, *Phys. Rev. C* **87**, 065503 (2013).
- [68] MAID Collaboration, <http://www.kph.uni-mainz.de/MAID> (2011).
- [69] T. Leitner, L. Alvarez-Ruso, and U. Mosel, *Phys. Rev. C* **73**, 065502 (2006).
- [70] M. Elkins *et al.* (MINERvA Collaboration), arXiv:1901.04892 [Phys. Rev. D (to be published)].
- [71] N. Tagg *et al.* (MINERvA Collaboration), *Nucl. Instrum. Methods Phys. Res., Sect. A* **676**, 44 (2012).
- [72] E. J. Moniz, I. Sick, R. R. Whitney, J. R. Ficenec, R. D. Kephart, and W. Trower, *Phys. Rev. Lett.* **26**, 445 (1971).

- [73] J. W. Van Orden and T. W. Donnelly, *Ann. Phys. (N.Y.)* **131**, 451 (1981).
- [74] A. A. Aguilar-Arevalo *et al.* (MiniBooNE Collaboration), *Phys. Rev. D* **83**, 052007 (2011).
- [75] G. D'Agostini, *Nucl. Instrum. Methods Phys. Res., Sect. A* **362**, 487 (1995).
- [76] See Supplemental Material at <http://link.aps.org/supplemental/10.1103/PhysRevD.100.052008> for cross-section data points, their systematic uncertainties and correlations, and the $\bar{\nu}_\mu$ flux of the exposure as tables.
- [77] L. Fields, J. Chvojka *et al.* (MINERvA Collaboration), *Phys. Rev. Lett.* **111**, 022501 (2013).
- [78] F. Binon, P. Duteil, J. P. Garron, J. Gorres, L. Hugon, J. P. Peigneux, C. Schmit, M. Spighel, and J. P. Stroot (CERN-IPN (Orsay) Collaboration), *Nucl. Phys.* **B17**, 168 (1970).
- [79] D. Rein, *Nucl. Phys.* **B278**, 61 (1986).
- [80] A. Aguilar-Arevalo *et al.* (MiniBooNE Collaboration), *Phys. Rev. D* **83**, 052009 (2011).
- [81] P. Adamson *et al.* (MINOS Collaboration), *Phys. Rev. D* **91**, 012005 (2015).
- [82] O. Benhar and D. Meloni, *Phys. Rev. D* **80**, 073003 (2009).
- [83] J. Nieves, J. E. Amaro, and M. Valverde, *Phys. Rev. C* **70**, 055503 (2004); **72**, 019902(E) (2005).
- [84] M. Martini, M. Ericson, G. Chanfray, and J. Marteau, *Phys. Rev. C* **80**, 065501 (2009).
- [85] J. Marteau, *Eur. Phys. J. A* **5**, 183 (1999).
- [86] K. M. Graczyk and J. T. Sobczyk, *Eur. Phys. J. C* **31**, 177 (2003).
- [87] N. J. Baker, A. M. Cnops, P. L. Connolly, S. A. Kahn, M. J. Murtagh, R. B. Palmer, N. P. Samios, and M. Tanaka, *Phys. Rev. D* **23**, 2495 (1981).
- [88] G. M. Radecky *et al.*, *Phys. Rev. D* **25**, 1161 (1982).